Critical issues on coherent interface energy calculations revisited: The case of Al/TiB2

Rémy Besson, Sabrina Macaluso, Ludovic Thuinet

Critical issues on coherent interface energy calculations revisited: the case of Al/TiB_2

R. Besson[†,‡], S. Macaluso[†], and L. Thuinet[†]

[†]Univ. Lille, CNRS, INRAE, Centrale Lille, UMR 8207 - UMET - Unité Matériaux et Transformations, F-59000 Lille, France
[‡]Corresponding author: Tel: +33 (0) 320 33 62 25 / Fax: +33 (0) 320 43 65 91, e-mail: Remy.Besson@univ-lille.fr

July 11, 2022

Keywords : DFT - coherent interface - metal/ceramic interface - chemical potential - elastic theory

Abstract

Properties of Al/TiB_2 heterophase interfaces are investigated by means of atomic-scale calculations. Focusing on practically important $(111)_{Al}$ // $(0001)_{TiB_2}$ basal interfaces, our study allows to clarify various ambiguities present in the literature when calculating coherent interface energies in non-binary systems: (i) while neglected in earlier works on Al/TiB_2, elasticity effects are properly taken into account, (ii) a critical point determining interface stability being related to chemical potentials in ordered compounds, their ranges of values are determined by a careful analysis ensuring TiB_2 stability and absence of undesired other phases, and (iii) comparing different simulation systems leads to conclude that periodic boundary conditions should be preferred to free surface ones, frequently used in earlier studies. This work is the first attempt to bring the improvements (i) to (iii) in the same methodology and allows to obtain more realistic values of coherent interface energies than those previously available in the literature.

1 Introduction

Due to their beneficial strength/weight ratio, aluminium alloys are of high interest in many areas such as aeronautics, automotive or cutting tools industries. The properties of Al alloys are enhanced by addition of TiB_2 [1–3], a compound characterized by a high melting point (3173 K), hardness (2500 HV) and Young modulus (565 GPa). A recent experimental study [2] revealed that 7075 Al alloys reinforced by TiB_2 nanoparticles present a total elongation to failure of around 15% and a tensile strength of 677 MPa, namely higher than previously measured [4–9]. It was suggested [2] that these improved properties are related to the atomic structure of the Al/TiB_2 basal interfaces frequently present in the microstructure. Various misfit dislocation densities have been reported at Al/TiB_2 interfaces, depending on the orientation of the TiB_2 facet. Indeed, $(0001)_{TiB_2}$ basal facets present a moderate misfit (6.27%), while misfits are much higher ($\geq$ 30%) for $(01\bar{1}1)_{TiB_2}$ pyramidal and $(01\bar{1}0)_{TiB_2}$ prismatic facets, a feature associated respectively with coherent and semi-coherent Al/TiB_2 interfaces. This dependence of the degree of coherency on interface orientation is likely to induce intricate interface properties. They are frequently investigated by means of atomic-scale simulation and modelling, since these approaches conveniently allow to estimate interface structures and excess (free) energies, the latter being key-parameters for interface stability.

While such atomic-scale investigations are relatively straightforward for stress-free incoherent interfaces (e.g. grain boundaries...), the level of intricacy raises significantly in the case of coherent interfaces, because the excess energy then not only reflects local interface effects, but must also include an elastic contribution due to the deformation of both phases induced by coherency. While a reduced panel of heterophase coherent interfaces have already been investigated from theory and simulation [10], it should be noted that considerable ambiguities still currently exist among these available studies. Considering first binary systems to which the majority of these works were devoted, these studies can be divided into two groups, depending on the treatment of elasticity effects. As regards works ignoring elasticity, the earliest one is related to Al/Al_2Cu-θ' interfaces [11] . Their energies were determined by molecular dynamics with a modified-embedded-atom method (MEAM) potential and periodic boundary conditions (PBC), leading to energies equal to 156 and 694 mJ/m^2 for coherent and semi-coherent interfaces respectively. Similarly, Ni/Ni_3Al coherent interfaces with a 1.3% mismatch were studied using molecular dynamics with EAM potentials [12] and PBC systems. Coherent interface energies in Ni/Ni_3Al were found to lie in the range 290-312 mJ/m^2, two terminations (namely either pure Ni or mixed Ni-Al) were possible for the Ni_3Al side of the interface, leading to ambiguities on the possible interface configurations. Turning towards works on binary systems in which elasticity effects were taken into account, they adopted the same approach, namely subtracting the elastic part to the excess energy in PBC multilayered systems. In this context, the Al/Al_2Cu-θ' system, with 0.68% and 5.1% mismatch for coherent and semi-coherent interfaces [13,14], was investigated by ab initio calculations, and interface energies respectively equal to 235 and 615 mJ/m^2 were found. To conclude this survey of coherent interfaces in binary systems, metal-hydride Zr/H-Zr interface energies were also determined by ab initio calculations. For the fully coherent γ' (ZrH) hydride, the basal (respectively prismatic) interface energy was assessed at 65 mJ/m^2 (respectively 35 mJ/m^2) while for the ζ phase, the prismatic interface energy was of 35 mJ/m^2 and the basal one very close to 0 [15]. All these values were quite low, certainly due to the fact that these phases and the Zr matrix have close crystallographic structures. A similar study was performed with the γ-ZrH compound [16]. Since it is tetragonal, it forms basal coherent interfaces with the matrix, but contains a network of Shockley partials in its semi-coherent prismatic interfaces. The obtained energies were in the range 170-200 mJ/m^2 and 700-750 mJ/m^2 for the coherent and semi-coherent cases respectively.

When tackling interfaces in non-binary systems, one is faced with a somewhat more intricate situation, especially visible for aspects related to thermodynamics, the presence of (at least) three chemical elements and only two phases making it difficult to settle precisely the equilibrium to which the interface should be subjected. Due to this complexity, only few non-binary coherent interfaces have been concerned with atomic-scale simulation studies up to now, namely (to the authors' knowledge) Al/Mg_5Si_6, Al/SiO_2, Mg/TiB_2 and Al/TiB_2 [17–21]. For Al/Mg_5Si_6, the methodology adopted was mostly similar to that followed in earlier works on binary cases, at least those including proper separation of strain and interface energies. On the other hand, the thermodynamic treatment was simplified by restrictive use of simulation systems containing integer numbers of Mg_5Si_6 unit cells. While this assumption offers the advantage that interface energies become independent of alloy composition, it may imply in general that the selected interface configurations are insufficiently optimized. To overcome this difficulty, a slightly different approach was employed in previous works on TiB_2 or SiO_2. Considering for instance TiB_2, since the stability of this ordered compound depends on the Ti and B chemical potentials, usually unknown in practice, these quantities were therefore kept as control parameters, constrained to lie within an interval consistent with TiB_2 stability. While this framework, employed for all previous works on Al/SiO_2, Mg/TiB_2 and Al/TiB_2 [18–21], is rigorous and general, its practical interest is however somewhat reduced by the fact that it no longer provides single values, but only ranges with significant widths, for interface energies, making it difficult to determine which interface configuration should be preferred in each case. Apart from thermodynamics,

several debatable questions should be pointed out in these earlier works on coherent interfaces in Al/SiO_2, Mg/TiB_2 and Al/TiB_2. Concerning interfaces in Al/SiO_2, in the single earlier study available [18], using ab initio calculations and free surface conditions (FSCs), the low mismatch (1%) in this system led the authors to assume that the elastic contribution can be completely ignored, an assumption which however should deserve further checking. Moreover, this work contains other unresolved issues, related to the termination of the SiO_2 side of the interface: three kinds of terminations (Si, one-O or two-O) being a priori possible, only the one-O termination was considered (for tractability reasons) in the interface study, a choice however questionable because the SiO_2 (0001) surface with two-O termination was pointed out as the most stable one in the same study. Depending on the O chemical potential, coherent interface energies in Al/SiO_2 were found to lie in the range 1.35-1.44 J/m^2. As concerns a similar work performed recently on Mg/TiB_2 [19] using ab initio calculations and FSC systems, the authors considered two possible terminations (either Ti or B) for the TiB_2 side, resulting in interface energies in the range 1.65-5.08 J/m^2. As for Al/SiO_2, the contribution of elasticity was not taken into account, although the Mg/TiB_2 interfaces were supposed fully coherent with a significant mismatch (5.6%). Considering the last non-binary system investigated hitherto, namely Al/TiB_2, similar coherent interface energy calculations are reported in two studies relying both on FSC systems, leading to values in the range $1.03 - 3.23$ J/m^2 [20] and $1.00 - 2.86$ J/m^2 [21]. It is worth noting that, in the first [20] of these two works on Al/TiB_2 interfaces, the simulation systems used involved a single interface (together with Al and TiB_2 free surfaces, i.e boundary conditions labelled FSC1 below), contrary to the second work [21] which involved two non-identical interfaces (with only Al free surfaces, i.e. boundary conditions labelled FSC2 below), questioning the validity of the resulting Al/TiB_2 interface energies. Most noticeably, in all these earlier works devoted to Al/SiO_2, Mg/TiB_2 and Al/TiB_2, interface energies were never found lower than 1000 mJ/m^2, i.e. a surprisingly high energy bottom level for coherent interfaces.

This illustrates the difficulty to consider exhaustively all the possible interfaces in both binary and non-binary systems. However, some works attempted to reduce this complexity with some assumptions on nucleation. Works on the properties of Al/TiB_2 interfaces have been performed [22, 23] in which Al was melted by ab initio molecular dynamics calculations. The authors of both studies compared two simulations depending on the termination of TiB_2 (Ti-terminated or B-terminated) and investigated the structural properties of these interfaces. They drew the same conclusions, namely that Ti-terminated surface possesses a better layering order of Al toward its crystallization state than B-terminated surface suggesting that Ti-terminated surface is more favorable to Al nucleation. In another work [24], it is reported that the Ti-terminated surface of TiB_2 is guaranteed by a Ti-rich chemical potential in the system suggesting that Al/TiB_2 interfaces could be studied in Ti-rich conditions.

To sum up, this overview of the previous works dedicated to atomic-scale simulations of coherent interfaces emphasizes several methodological issues as well as ambiguities on the predicted interface properties. Concerning more specifically our subject of interest in this work, namely the Al/TiB_2 basal interfaces previously investigated in the couple of works [20, 21], these issues can be listed as follows:

1. Elasticity was not taken into account in these works.
2. As a consequence, abnormally high energies were proposed for coherent interfaces in Al/TiB_2.
3. There are ambiguities on the selection and geometrical analysis of interface configurations.
4. Different kinds of boundary conditions (PBC or FSC) were used to perform the simulations, leading to somewhat conflicting results, and without any information on the respective merits of either choice.

Table 1. Geometrical configurations of Al/TiB_2 basal interfaces (with α=Al and β=TiB_2). FCC Al has an ABC stacking sequence while HCP TiB_2 possesses an AB* stacking sequence, B* indicating positions B and C.

Configuration	Stacking sequence		
I1	$A_\alpha B_\alpha C_\alpha A_\alpha$ / $A_\beta\{B_\beta{+}C_\beta\}A_\beta$		
I2	$C_\alpha A_\alpha B_\alpha$ / $A_\beta\{B_\beta{+}C_\beta\}A_\beta$		
I3	$B_\alpha C_\alpha A_\alpha B_\alpha C_\alpha$ / $A_\beta\{B_\beta{+}C_\beta\}A_\beta$		
I4	$A_\alpha B_\alpha C_\alpha A_\alpha$ / $\{B_\beta{+}C_\beta\}A_\beta\{B_\beta{+}C_\beta\}$		
I5	$C_\alpha A_\alpha B_\alpha$ / $\{B_\beta{+}C_\beta\}A_\beta\{B_\beta{+}C_\beta\}$		
I6	$B_\alpha C_\alpha A_\alpha B_\alpha C_\alpha$ / $\{B_\beta{+}C_\beta\}A_\beta\{B_\beta{+}C_\beta\}$		
I7	$A_\alpha C_\alpha B_\alpha A_\alpha$ / $A_\beta\{B_\beta{+}C_\beta\}A_\beta$	$\xRightarrow{\mathscr{R}_A}$	I1
I8	$B_\alpha A_\alpha C_\alpha$ / $A_\beta\{B_\beta{+}C_\beta\}A_\beta$	$\xRightarrow{\mathscr{R}_A}$	I2
I9	$C_\alpha B_\alpha A_\alpha C_\alpha B_\alpha$ / $A_\beta\{B_\beta{+}C_\beta\}A_\beta$	$\xRightarrow{\mathscr{R}_A}$	I3
I10	$A_\alpha C_\alpha B_\alpha A_\alpha$ / $\{B_\beta{+}C_\beta\}A_\beta\{B_\beta{+}C_\beta\}$	$\xRightarrow{\mathscr{R}_A}$	I4
I11	$B_\alpha A_\alpha C_\alpha$ / $\{B_\beta{+}C_\beta\}A_\beta\{B_\beta{+}C_\beta\}$	$\xRightarrow{\mathscr{R}_A}$	I5
I12	$C_\alpha B_\alpha A_\alpha C_\alpha B_\alpha$ / $\{B_\beta{+}C_\beta\}A_\beta\{B_\beta{+}C_\beta\}$	$\xRightarrow{\mathscr{R}_A}$	I6

In this intricate context, the aim of the present work is to properly investigate Al/TiB_2 basal interfaces by ab initio calculations, which requires to clarify points 1 to 4 above. Section 2 settles the methodological aspects required for this interface study. In particular, a detailed structural analysis is carried out, leading to a proper set of candidate configurations for Al/TiB_2 interfaces, together with a thermodynamic analysis of the role of Ti and B chemical potentials. Using these tools, section 3 is devoted to the Al/TiB_2 basal coherent interface study using multilayered systems with various boundary conditions and rigorous handling of elasticity. Finally, in section 4, important issues are discussed, such as the respective effects of elasticity and boundary conditions, as well as the comparison of our results with earlier ones available in the literature.

2 Methodology

2.1 Details on ab initio calculations

In the present work, first-principles calculations are carried out with the Vienna Ab Initio Simulation Package (version VASP.5.4.1). The generalized gradient approximation (GGA) [25] in the Perdew-Burke-Ernzerhof (PBE) [26] functional form is used for the description exchange-correlation. The plane wave cut-off energy is selected as 500 eV. The Gamma point centered scheme and the Monkhorst-Pack mesh [27] are used for Brillouin zone sampling for the bulk and interface calculations. The k-grids used are respectively 18×18×n (with $n \in [1, 3]$), 16×16×16 and 18×18×18 for the Al/TiB_2 interfaces, bulk TiB_2 and Al. All energy minimizations include the optimization of atomic positions as well as supercell shape and volume. The total energy is calculated using the tetrahedron method with Blöchl [28] corrections, convergence to values lower than 10^{-3} eV/atom being ensured. For Ti, B and Al, the valence electrons considered in the pseudo-potentials are $3s^2 3p^6 3d^2 4s^2$(Ti), $2s^2 2p^1$ (B) and $3s^2 3p^1$ (Al). Atomic structures are visualized with VESTA (Visualisation for Electronic and Structural Analysis) [29].

2.2 Bulk properties and stability of TiB_2

The lattice parameters and elastic constants of the TiB_2 and Al bulk phases with space groups P6/mmm and Fm-3m respectively are calculated and reported in Tables A.1, A.2 and A.3. For

TiB_2, the calculated lattice parameters are $a^{eq}_{TiB_2} = 3.036$ Å and $c^{eq}_{TiB_2} = 3.232$ Å, which is consistent with experimental data ($a^{eq}_{TiB_2} = 3.023 - 3.036$ Å and $c^{eq}_{TiB_2} = 3.226 - 3.231$ Å [30]). For FCC Al, the calculated lattice parameter is $a^{eq}_{Al} = 4.0409$ Å which is also in complete agreement with the experimental data $a^{eq}_{Al} = 4.04145$ Å [31]. The reference energy of FCC Al is E^{Al}_{Ref}=-3.745 eV/atom. The formation energies H_f in eV of the various Al-Ti-B phases X_iY_j, with X,Y=Ti,B or Al are calculated as:

$$E_f(X_iY_j) = (i+j)E^{X_iY_j}_{Ref} - iE^{X}_{Ref} - jE^{Y}_{Ref} \tag{1}$$

where i and j stand for the numbers of X and Y atoms respectively, while E_{Ref} corresponds to the total energy per atom of the supercell after relaxation to zero pressure. To get the bulk energies of titanium and boron, α-B12 and α-Ti are chosen. The formation energy of TiB_2 calculated in this work is -3.178 eV which is consistent with [20, 21, 32]. The formation energy of Al_3Ti is -1.594 eV, which fits the experimental [33–35] or theoretical values [20, 21]. The formation energy of AlB_2 is also in good agreement with theoretical data [20,21,32], with a value of -0.135 eV.

In interface calculations, chemical potentials are needed (see below). In previous works [20,21], the conditions for the stability of TiB_2 were determined only by considering the absence of α-Ti and α-B12 phases. However from experiments [3], AlB_2 and Al_3Ti do not form either, and therefore, these phases are also taken into account in our work in order to ensure that their presence is effectively forbidden in the thermodynamic treatment. On the whole, the range of stability of TiB_2 avoiding the formation of AlB_2, Al_3Ti, α-Ti and α-B12 is expressed as a function of $\Delta\mu_{Ti} = \mu^{TiB_2}_{Ti} - E^{\alpha\text{-Ti}}_{Ref}$ by the following equation (Appendix B):

$$H_f(TiB_2) - H_f(AlB_2) \leq \Delta\mu_{Ti} \leq H_f(Al_3Ti) \tag{2}$$

which, for the ab initio energetics used here, yields numerically:

$$-3.043eV \leq \Delta\mu_{Ti} \leq -1.594eV \tag{3}$$

Equation (3) defines the range of stability of the TiB_2 compound.

2.3 Geometrical analysis of Al/TiB_2 basal interfaces

From experiments [3, 36–38], the most commonly accepted orientation relationships (OR) for Al/TiB_2 basal interfaces is:

$$(111)_{Al}//(0001)_{TiB_2}, [1\bar{1}0]_{Al}//[11\bar{2}0]_{TiB_2} \tag{4}$$

Hence, our work is carried out by using this OR to construct the Al/TiB_2 interfaces which yields the following correspondence between Al and TiB_2 crystallographic directions (Figure 1):

$$\begin{cases} \frac{1}{2}[1\bar{1}0]_{Al} \;//\; \frac{1}{3}[11\bar{2}0]_{TiB_2} \\ \frac{1}{2}[11\bar{2}]_{Al} \;//\; [\bar{1}100]_{TiB_2} \\ \frac{1}{3}[111]_{Al} \;//\; \frac{1}{2}[0001]_{TiB_2} \end{cases} \tag{5}$$

The $(0001)_{TiB_2}$ and $(111)_{Al}$ planes are in epitaxial correspondence, Al is the most deformable phase, indeed its elastic constants are much smaller than those of TiB_2 (Appendix A.1, Tables A.2 and A.3). The calculation of the coherency mismatch between Al and TiB_2 leads to a value of 6.45% (Appendix A.2). For the FCC Al phase, the stacking sequence of $(111)_{Al}$ is an ABC arrangement, while HCP TiB_2 yields an AB stacking sequence of $(0001)_{TiB_2}$ planes. Therefore, the numbers of permutations of layers for Al and TiB_2 are 3! and 2! respectively,

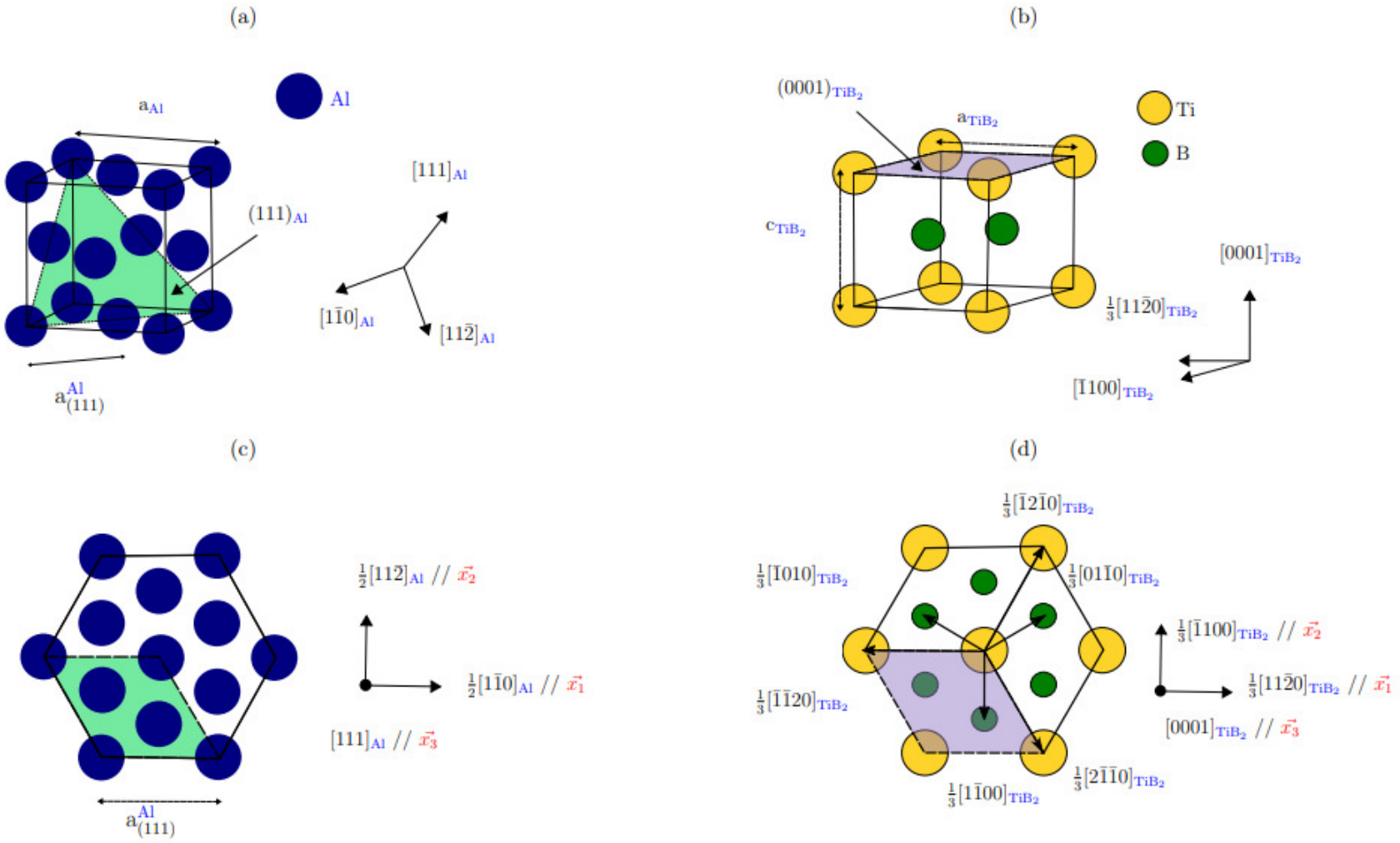

Figure 1. Crystallographic structures of (a) Al and (b) TiB_2 bulk phases. Basal projections of (c) Al along the $[111]_{Al}$ direction and (d) TiB_2 along the $[0001]_{TiB_2}$ direction. The shadowed diamonds in (c) and (d) are in epitaxial correspondence. ($\vec{x_1}$,$\vec{x_2}$,$\vec{x_3}$) is the orthonormal basis used to perform the elasticity calculations (Appendix A).

Table 2. Comparison between the configurations of Al/TiB_2 basal interfaces in our work and those proposed in [20, 21]. Configurations for which the interface energy is calculated are highlighted in green. The configurations are categorized according to the Ti- and B-termination planes at the interface. The question marks stand for ambiguities on the configuration labelling ([20]).

	This work	Han et al. [20]	Deng et al. [21]
Ti-terminated	I1 I2, I3 →	OT Ti ? HCP Ti	OT Ti ← HCP Ti FCC Ti
	MT Ti	MT Ti	MT Ti
B-terminated	I4 I5, I6 →	HCP B ? OT B	OT B ← HCP B FCC B
	MT B1 MT B2	MT B -	- MT B

which leads to an initial set of 12 configurations listed in Table 1. However, by considering specific symmetry operations, this initial set can be reduced. Indeed, the π rotation $\mathscr{R}_A$ around an axis perpendicular to the basal plane $(111)_{Al}$ // $(0001)_{TiB_2}$ and passing through an atom of the A layer exchanges B and C positions while the A positions remain unchanged. This rotation $\mathscr{R}_A$ transforms configurations from I7 to I12 to configurations from I1 to I6. In Table 2, these different configurations are compared to the ones proposed previously in works [20, 21]: three new configurations (MT Ti, MT B1 and MT B2) should be added to the present work, resulting from rigid-body translations within the interface plane and ignored in our geometrical analysis. This comparison highlights several ambiguities on interface configurations. Firstly, the earlier configuration labellings may be confusing (HCP B from [20] corresponds to OT B from [21], whereas HCP B from [21] corresponds to OT B from [20]). Moreover, the description used by [20] leads to uncertain configurations. For instance, it is unclear whether HCP Ti from [20] corresponds to HCP Ti or FCC Ti from [21] and to I2 or I3 in our present work. In a similar way, OT B from [20] may correspond to HCP B or FCC B in [21] and to I5 or I6 in our work. To remedy this deficiencies, we thus found necessary, to investigate interface energies for the whole set of configurations identified and listed in the first column of Table 2. It must be emphasized that in [20, 21], interface energies were performed only for two configurations (HCP Ti and HCP B). This point will be discussed in more details in Section 4.

2.4 Energies of Al/TiB_2 multilayers

To get appropriate interface energies, the elastic contribution should be subtracted from the excess energy, defined as the difference between the total energy of the system containing the interface and the energies of the bulk phases. To tackle this issue, the most seemingly reliable method [16] consists in using multilayers, for which the excess energy noted $\Delta E_{multi}(p, \chi)$ depends on the total (including both phases) number p of Al, Ti or B layers used and the volume fraction χ of the TiB_2 phase ($\chi = \frac{V_{TiB_2}}{V_{Al}+V_{TiB_2}}$ where V_{TiB_2} and V_{Al} stand for the volumes of the TiB_2 and Al phases in the supercell). $\Delta E_{multi}(p, \chi)$ is expressed by:

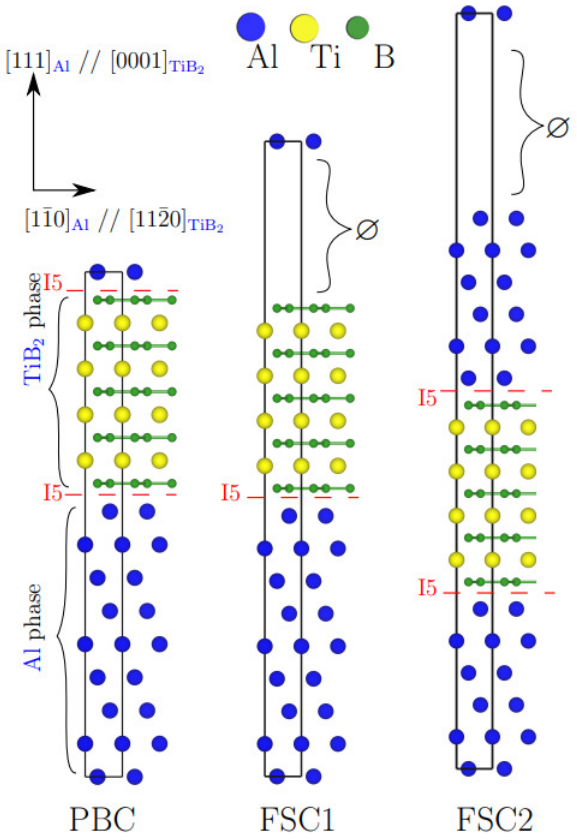

Figure 2. Illustration of the three types of boundary conditions (PBC, FSC1, FSC2) adopted in this work in the case of the I5 configuration. The red dashed lines indicate the Al/TiB_2 interface positions.

$$\Delta E_{\text{multi}}(p,\chi) = E_{\text{tot}}^{\text{Al/TiB}_2} - \sum_i n_i \mu_i \tag{6}$$

$$= E_{\text{tot}}^{\text{Al/TiB}_2} - n_{\text{Al}} E_{\text{Ref}}^{\text{Al}} - n_{\text{Ti}} \mu_{\text{Ti}}^{\text{TiB}_2} - n_{\text{B}} \mu_{\text{B}}^{\text{TiB}_2} \tag{7}$$

with $E_{\text{tot}}^{\text{Al/TiB}_2}$ the total energy of the system containing the Al/TiB_2 interface after relaxation and n_{i} the number of atoms of type i in the system. All theses quantities depend on p and χ. As outlined above, three different types of supercell have been adopted to assess this excess energy according to the literature. The first type of supercell labelled PBC contains one slab of Al and one slab of TiB_2 without any vacuum and is periodic in each direction. The second one, labelled FSC1, also contains one slab of Al and one slab of TiB_2 with vacuum at the extremity of each slab and then involves free surfaces of Al and TiB_2. This supercell is similar to the one employed in [20]. Finally, the third one contains one block of TiB_2 between two blocks of Al in contact with vacuum, this supercell being used in work [21] and labelled FSC2 in the following. These three types of supercell are used in this work and represented in Figure 2.

$\Delta E_{\text{multi}}(p,\chi)$ can be divided into several contributions: the elastic energy $e_{\text{el}}(\chi)pV_l$, with e_{el} the elastic energy density and V_l the average volume of one layer, the interface energy σ and, depending on the type of supercell considered, the Al or TiB_2 free surface energies. The following expressions (8) to (10) describe this additive energy decomposition of the multilayer excess energy for the various systems (PBC, FSC1 or FSC2):

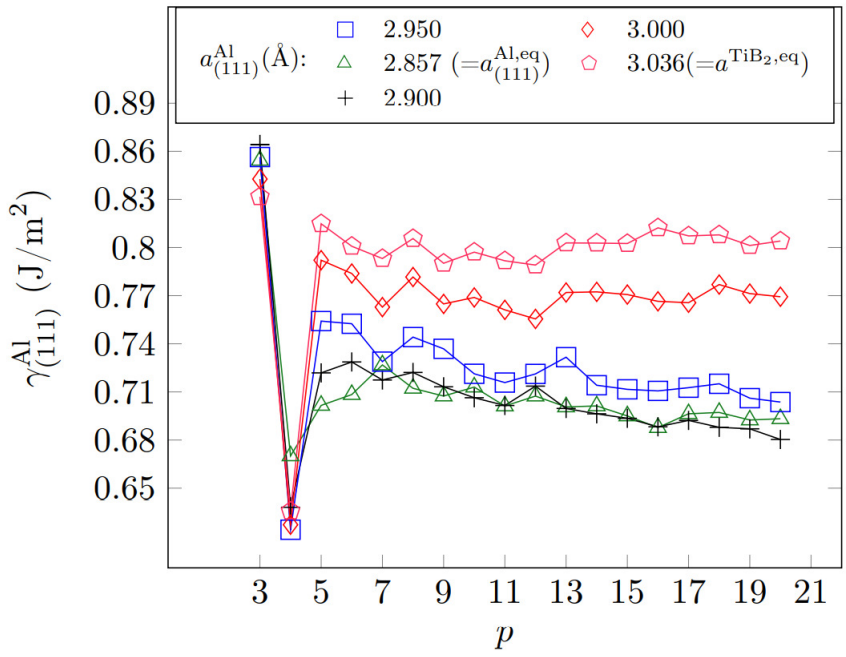

Figure 3. Surface energy of $(111)_{\mathrm{Al}}$ as a function of the number p of layers, depending on the basal lattice parameter $a^{\mathrm{Al}}_{(111)}$ defined in Figure 1.

$$\Delta E^{\mathrm{PBC}}_{\mathrm{multi}}(p,\chi) = 2A\sigma^{\mathrm{PBC}} + e_{\mathrm{el}}(\chi)pV_l \tag{8}$$

$$\Delta E^{\mathrm{FSC1}}_{\mathrm{multi}}(p,\chi) - A(\gamma^{\mathrm{Al}}_{(111)} + \gamma^{\mathrm{TiB_2}}_{(0001)}) = A\sigma^{\mathrm{FSC1}} + e_{\mathrm{el}}(\chi)pV_l \tag{9}$$

$$\Delta E^{\mathrm{FSC2}}_{\mathrm{multi}}(p,\chi) - 2A\gamma^{\mathrm{Al}}_{(111)} = 2A\sigma^{\mathrm{FSC2}} + e_{\mathrm{el}}(\chi)pV_l \tag{10}$$

where A is the area of a single $\mathrm{Al/TiB_2}$ interface in each simulated system, $\gamma^{\mathrm{Al}}_{(111)}$ and $\gamma^{\mathrm{TiB_2}}_{(0001)}$ being the free surface energies of $(111)_{\mathrm{Al}}$ and $(0001)_{\mathrm{TiB_2}}$ planes. From equations (8) to (10), after linear regression, interface energies can be extracted by extrapolating the left-hand term to $p = 0$, while the slope yields the elastic energy density in each case.

3 Results

3.1 Al and $\mathrm{TiB_2}$ surfaces

To study the FSC1 and FSC2 systems, that involve free surfaces, as shown in equations (9) and (10), the surface energies for Al and $\mathrm{TiB_2}$ must be determined beforehand.

The surface energy of each phase ϕ=(Al,$\mathrm{TiB_2}$) can be expressed as follows:

$$\gamma^{\phi} = \frac{1}{2A}(E^{\phi}_{\mathrm{tot}} - \sum_i n_i\mu^{\phi}_i) \tag{11}$$

where E^{ϕ}_{tot} stands for the total ab initio energy of the p-layer ϕ supercell with free surfaces, and μ^{ϕ}_i corresponds to the chemical potential of species i (Al, Ti or B) in phase ϕ. The surface energy is calculated for increasing numbers p of layers $(111)_{\mathrm{Al}}$ and $(0001)_{\mathrm{TiB_2}}$, in order to ensure a good convergence. In Figures 3 and 4, the surface energies of non-deformed Al ($a^{\mathrm{Al}}_{(111)} = a^{\mathrm{Al,eq}}_{(111)}$, see Figure 1) and $\mathrm{TiB_2}$ are reported and converge within 10 mJ/m^2 for $p = 19$ and $p = 15$

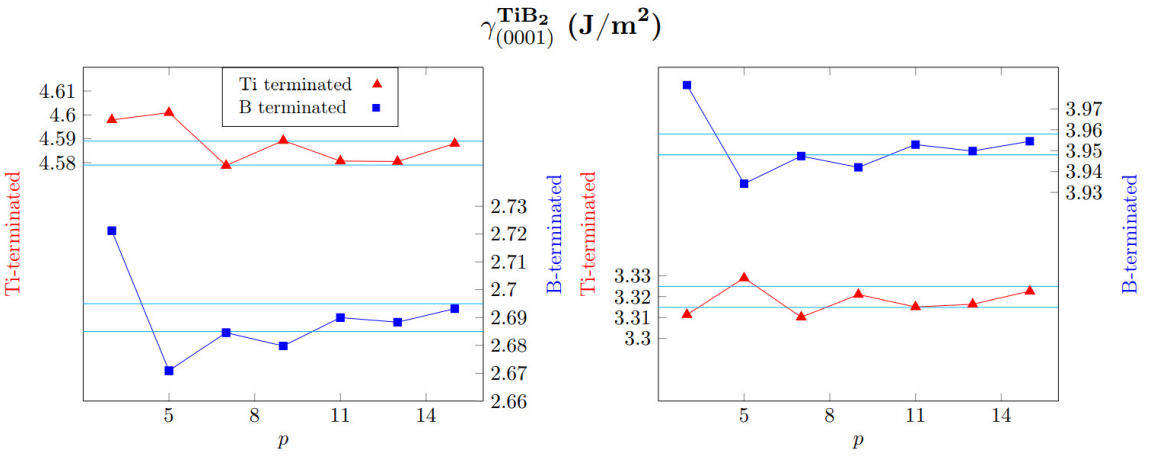

(a) B-rich conditions ($\Delta\mu_{Ti} = -3.043\ eV$) (b) Ti-rich conditions ($\Delta\mu_{Ti} = -1.594\ eV$)

Figure 4. Surface energies of TiB_2 as a function of the number p of layers, depending on the Ti or B terminations and $\Delta\mu_{Ti}$.

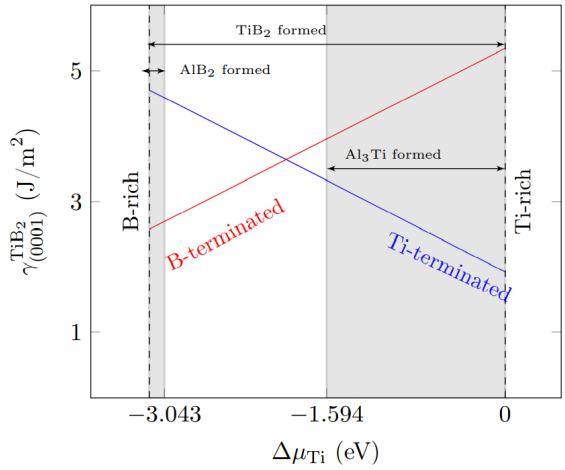

Figure 5. Surface energy $\gamma^{TiB_2}_{(0001)}$ of $(0001)_{TiB_2}$ as a function of $\Delta\mu_{Ti}$, for Ti and B terminations of TiB_2. The surface energy values are converged with the number p of layers (Figure 4). The non-shadowed zone indicates the TiB_2 range of stability (equation (3)).

respectively. For non-deformed Al, the surface energy of $(111)_{Al}$ planes is 0.693 J/m^2, which is different from previous evaluations (0.83 J/m^2 in [20] and 0.80 J/m^2 in [21]). TiB_2 surface energies depend on chemical potentials and are displayed in Figure 5, for the range of stability of this compound expressed in equation (3). The two surface terminations, either Ti or B of TiB_2, are studied. In B-rich conditions ($\Delta\mu_{Ti} = -3.043\ eV$), the Ti-terminated surface presents a higher energy (4.59 J/m^2) than the B-terminated surface (2.69 J/m^2), which indicates that the B-terminated surface is more favorable in these conditions. In Ti-rich conditions ($\Delta\mu_{Ti} = -1.594\ eV$), this is the contrary (3.95 J/m^2 for the B-terminated surface vs. 3.32 J/m^2 for the Ti-terminated surface).

3.2 Al/TiB_2 basal interfaces

The Al/TiB_2 basal interface energies for the three systems (PBC, FSC1 and FSC2) and the nine configurations of Table 2 are deduced from equations (8) to (10). As mentioned previously, the additive decomposition expressed by these equations, mandatory to take into account the elasticity, turned out to be adequate for various systems such as Al/θ'-Al_2Cu [13, 14] or Zr/H-Zr [16]. Since this approach was completely overlooked in previous works [20, 21], it is necessary to first check its applicability to this system. To this aim, ΔE_{multi} for MT Ti configuration (Table 2) in PBC systems is first calculated for several values of χ ($\chi = 0.18, 0.38, 0.68$) and for each an extensive set of p. As shown in Figure 6, linear dependency on p is in agreement with equation (8). In addition, the interface energy of MT Ti is not influenced by the TiB_2 volume fraction χ used (linear regressions give approximately the same value for $p = 0$).

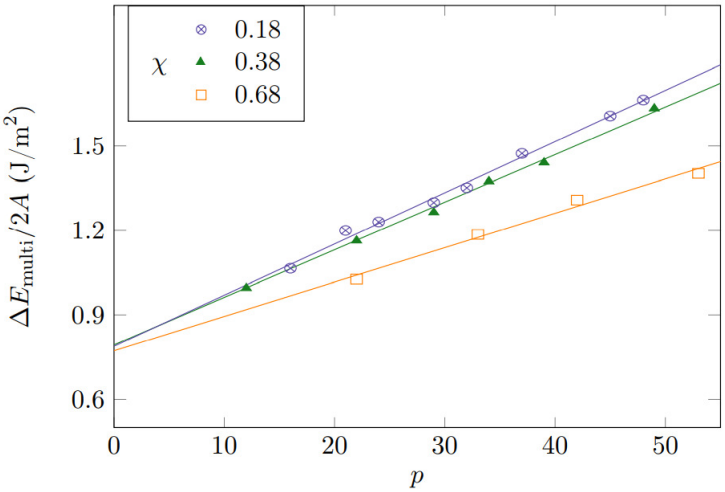

Figure 6. Ab initio energies of Al/TiB_2 basal interface multilayers for the MT Ti configuration (symbols), as a function of the number p of layers for various TiB_2 volume fractions χ, in the case of PBC systems and Ti-rich conditions ($\Delta\mu_{\text{Ti}} = -1.594eV$). The lines refer to the linear regression performed to obtain the interface energy.

In Figure 7a, ΔE_{multi} of PBC systems is plotted as a function of the total number of layers p for the nine configurations. The good linear dependency obtained for the nine configurations further confirms the adequacy of the method, at least when using PBC systems. The interface energies for PBC systems are then obtained after extrapolation to $p = 0$ from equation (8) to eliminate any elastic energy. These features, the linear dependency with p and the non-influence of the volume fraction χ on the interface energy, confirm that this approach is applicable for the Al/TiB_2 system, at least in PBC case.

It must be emphasized that the linear dependency with p of the left-hand terms in equations (8) to (10) is ensured if the slope $e_{\text{el}}(\chi)V_l$ is constant, i.e. if the TiB_2 volume fraction χ is constant. For the calculations, χ is then maintained at the same value for each configuration in order to perform linear regressions and obtain interface energies. The volume fraction χ lies between 0.32 and 0.45 for PBC and FSC1 systems and between 0.24 and 0.49 for FSC2 ones. χ values are selected in order to get supercells as small as possible. For FSC2 systems, due to an extra slab of Al, χ could not be at the same values as for the PBC and FSC1 systems. For PBC and FSC1 systems, from 5 to 8 supercells are used depending on the configuration, for a total number of layers p varying between 12 and 49. For FSC2 systems, from 2 to 4 supercells are employed for p between 13 and 51. In Figures 7b and 7c, as for PBC, the FSC1 and FSC2 systems also show a good linear dependency with p.

In the range of stability of TiB_2 (equation (3)), the interface energies σ^{PBC} deduced from the PBC systems present two distinct behaviors depending on the Ti chemical potential in the TiB_2 phase, as shown in Figure 8. In Ti-rich conditions, the Ti-terminated configurations have smaller interface energies than the B-terminated configurations which means that Ti-terminated configurations are more stable than B-terminated ones, also reported for surface energies previously in this work (see Section 3.1). Irrespective to $\Delta\mu_{Ti}$, the interface energy value of configuration I1 is much higher (up to 1600 mJ/m^2) than other Ti-terminated ones that are extremely close to each other, which excludes I1 from favorable configurations. However, in B-rich conditions, B-terminated configurations possess lower interface energies than Ti-terminated ones indicating that B-terminated configurations are more favorable. The interface energies for these configurations are close to each other, yet configurations MT B1 and I4 present superposed and the lowest interface energies that make them the most stable ones in B-rich conditions.

For each configuration, the interface energies in the range of stability of TiB_2 for the free surface systems, FSC1 and FSC2, were also determined which leads to figures similar to Figure 8 (thus not shown). They globally exhibit the same features as the ones obtained for PBC systems: (i) interface energies are between 1 and 4 J/m^2, (ii) the increasing and decreasing tendencies regarding the stability of these interfaces with chemical potentials remain identical, (iii) configuration I1 still exhibits the highest energy, making it the least favorable configuration compared to the other Ti-terminated configurations. However, some distinctions can be mentioned regarding the overall stability order of configurations for a given Ti or B termination: (i) the interface energy of configuration MT B1 becomes slightly lower (respectively higher) than I4 in FSC1 (respectively FSC2) compared to PBC systems, and in the same way (ii) the interface energy value of MT B2 is slightly higher (respectively lower) than I6 in FSC1 (respectively FSC2).

The interface energies deduced from PBC, FSC1 and FSC2 systems are reported in Tables 3a and 3b for the two limiting cases corresponding to the boundaries of the TiB_2 stability range expressed by equation (3): $\Delta\mu_{Ti} = -1.594\ eV$ (Ti-rich TiB_2 conditions) and $\Delta\mu_{Ti} = -3.043\ eV$ (B-rich TiB_2 conditions). Interface energies are first studied in Ti-rich conditions (Table 3a). For PBC systems, the uncertainty on the interface energies associated to the linear regression lies between 13 and 37 mJ/m^2, then it never exceeds a few % of interface energies. Configuration I1 has a much higher energy than the other configurations. If configuration I1 is excluded, two distinct clusters of configurations arise: Ti-terminated interfaces (I2, I3 and MT Ti) which possess lower interface energies than the B-terminated configurations (I4, I5, I6, MT B1 and MT B2). The lowest interface energy, 785 ± 17 mJ/m^2, is reached by configuration I2. Those results -(i) I1 not favorable, (ii) Ti-terminated configurations more stable in Ti-rich conditions- are also observed for the FSC1 and FSC2 systems. However, it should be mentioned that for FSC1, the most favorable configuration is MT Ti with an interface energy of 826 ± 240 mJ/m^2. Moreover, interface energies obtained in free surface systems are higher, by an amount between 53 and 324 mJ/m^2, than those obtained in PBC. The most stable configurations for PBC are from the most stable to the least stable I2, MT Ti and I3, which is very similar to the ones from FSC2 systems (most stable to the least stable : I2, I3 and MT Ti). For the FSC1 systems, the order of stability is first MT Ti followed by I3 and then I2.

We now consider interface energies in B-rich conditions (Table 3b). For PBC systems, the uncertainty of the linear regression lies between 14 and 40 mJ/m^2. Configuration I1 has the largest energy (3669 ± 40 mJ/m^2) in B-rich conditions also which confirms that this configuration is not likely to form. B-terminated configurations (I4, I5, I6, MT B1 and MT B2) possess lower energies than Ti-terminated configurations (I2, I3 and MT Ti). The lowest interface energy (547 ± 21 mJ/m^2) is obtained for configuration I4. As in Ti-rich conditions, results obtained for PBC systems in B-rich conditions are also confirmed by FSC1 and FSC2. However, it should be

Table 3. Interface energies σ (in mJ/m^2) of Al/TiB_2 basal interfaces for the nine configurations in Ti and B-rich conditions. For FSC1 and FSC2 systems, values are obtained for an Al surface energy $\gamma^{Al}_{(111)}$ of 0.693 J/m^2, which corresponds to non deformed bulk Al in Figure 3. Values in brackets correspond to those calculated in the literature.

(a) Ti-rich conditions ($\Delta\mu_{Ti} = -1.594\ eV$)

	Configuration	PBC	FSC1	FSC2
Ti-terminated	I1	2374 ± 37[a]	2583 ± 28	2364
	I2	785 ± 17	899 ± 39 (1450 [20])	784 ± 147 (1000 [21])
	I3	794 ± 18	849 ± 65	824 ± 31
	MT Ti	793 ± 13	826 ± 240	830 ± 44
B-terminated	I4	1838 ± 23	1994 ± 49 (3000 [20])	1875 ± 46
	I5	2028 ± 19	2160 ± 11	2104 ± 77 (2860 [21])
	I6	2155 ± 14	2279 ± 39	2228 ± 48
	MT B1	1845 ± 26	1960 ±17	1990 ± 2
	MT B2	2151 ± 34	2344 ± 70	2120 ± 271

a. Uncertainty of linear regression

(b) B-rich conditions ($\Delta\mu_{Ti} = -3.043\ eV$)

	Configuration	PBC	FSC1	FSC2
Ti-terminated	I1	3669 ± 40[a]	3952 ± 31	3652
	I2	2065 ± 17	2230 ± 45 (3228 [20])	2094 ± 163 (2826 [21])
	I3	2086 ± 20	2198 ± 71	2131 ± 32
	MT Ti	2085 ± 15	2176 ±251	2121 ± 22
B-terminated	I4	547 ± 21	649 ± 48 (1030 [20])	561 ± 49
	I5	749 ± 17	845 ± 11	800 ± 61 (1780 [21])
	I6	864 ± 14	947 ± 37	930 ± 46
	MT B1	555 ± 24	622 ±19	706 ± 8
	MT B2	863 ± 34	1010 ± 63	842 ± 270

a. Uncertainty of linear regression

Table 4. Elastic energy density $e_{el}(\chi)$ (J/cm^3) deduced from the linear regression with the total number of layers p (7) for each configuration of Al/TiB_2 basal interface in PBC, FSC1 and FSC2 systems.

	Configuration	PBC	χ	FSC1	χ	FSC2	χ
Ti-terminated	I1	173 ± 14	0.37	145 ± 6	0.37	176	0.49
	I2	155 ± 6	0.45	152 ± 9	0.45	205 ± 54	0.38
	I3	177 ± 7	0.33	190 ± 11	0.33	201 ± 9	0.24
	MT Ti	169 ± 5	0.37	212 ± 43	0.37	218 ± 4	0.30
B-terminated	I4	181 ± 6	0.37	166 ± 12	0.37	210 ± 14	0.29
	I5	171 ± 6	0.45	156 ± 2	0.45	186 ± 32	0.38
	I6	175 ± 4	0.33	182 ± 6	0.33	170 ± 13	0.38
	MT B1	188 ± 7	0.37	183 ± 3	0.37	162 ± 2	0.48
	MT B2	159 ± 9	0.37	155 ± 14	0.37	221 ± 90	0.48

mentioned that for FSC1, the most favorable configuration is MT B1 with an interface energy value of 622 ± 19 mJ/m^2. In B-rich conditions, the PBC and FSC2 systems share the same order of stability, from the most stable to the least stable configurations: I4, MT B1, I5, MT B2 and I6, while for FSC1 systems it is first MT B1 then I4, I5, I6 and finally MT B2. It is observed that interface energies for the couples (MT B1, I4), (MT B2, I6), and (MT Ti, I3) are close to each other.

For FSC2 systems, it should be noted that only few data points (between one and three values of p) are available. Indeed, FSC2 systems are larger than PBC or FSC1 ones due to an extra Al slab (Figure 2). Moreover, additional constraints to keep a constant TiB_2 volume fraction χ lead to even larger supercells along the direction perpendicular to the interface. These fewer points lead to a higher uncertainty of the linear regression. Moreover, the higher uncertainty obtained in FSC1 and FSC2 may also be explained by the surface energies of Al and TiB_2 used in the calculations (equations (9) and (10)). This will be discussed in Section 4.

3.3 Comparison with micro-elasticity theory

The previous analysis in Section 3.2 proves the reliability of the additive decomposition of multilayers energy (equations (8) to (10)) for Al/TiB_2 basal interfaces. However, it may be instructive to compare elastic energy densities $e_{el}(\chi)$ from the above DFT results with their counterparts deduced from micro-elasticity theory (μE) in order to investigate respective adequacy between this theory and the various PBC, FSC1 and FSC2 systems. The elastic energy density obtained analytically from μE (Appendix A, equation (A.21)) is calculated using as input the lattice parameters and elastic constants of the Al and TiB_2 phases indicated in Tables A.1, A.2 and A.3. $e_{el}(\chi)$ is plotted in Figure 9 and compared with the simulated data for each system and configuration as a function of the volume fraction χ. The μE elastic energy density reaches a maximum value for $\chi = 0.29$ of $e_{el} = 235.5$ J/cm^3. In spite of the dispersion, it seems that the DFT elastic energy density follows reasonably the μE prediction. Within the Al/TiB_2 interface, $a^{Al}_{(111)}$ and a_{TiB_2} (Figure 1) are equal to a common in-plane lattice parameter noted (a_{int}) due to coherency. From μE, it is also possible to determine the analytic expression of a_{int} as a function of the volume fraction χ (Appendix A, equation (A.27)), which is compared to its DFT counterpart in Figure 10. It should be noted that for $\chi = 0$ the lattice parameter a_{int} corresponds to the perfect FCC Al, i.e. $a^{eq}_{Al}/\sqrt{2} = 2.86$ Å while for $\chi = 1$, it corresponds to $a^{eq}_{TiB_2}$. The data from ab initio calculations are slightly lower than the data obtained from μE

theory. Yet the tendency of both data sets remains similar which suggests that our results are in good agreement with the elasticity theory. Moreover, the PBC system provides data closer to the elastic theory than free surfaces ones emphasizing its better reliability.

Table 4 provides a comparison of elastic energy density for the various systems used previously and calculated from the linear regressions represented in Figure 7. Since the bulk properties must not depend on the system, the same elastic energy density is expected in PBC, FSC1 and FSC2 cases. For PBC systems, the errors due to linear regression are small and lie between 4 and 14 J/cm^3. The elastic energy density from PBC systems is first compared with the FSC1 ones since both share similar volume fractions χ. FSC1 presents higher errors up to 43 J/cm^3 (20% of the elastic energy density). Taking into account errors induced by the linear regression, for all configurations, PBC and FSC1 systems show good agreement on $e_{\text{el}}(\chi)$ except for configurations I1 and I5. However, for FSC2 systems, due to fewer points used in the linear regression, the uncertainty is higher (up to 90 J/cm^3) than for previous systems. It should be mentioned that varying TiB_2 volume fraction χ leaves the interface energy unchanged (Figure 6) but changes the slopes of the linear regressions and thereby modifies the elastic energy density (equations (8) to (10)). Hence, the good consistency obtained in comparing FSC1 and PBC elastic energy densities is understandable, while the mismatch between FSC2 systems and previous PBC and FSC1 systems can be explained by the different TiB_2 volume fraction χ used. On the whole, the elastic energy densities for all the systems are similar if the error bars and the effect of the volume fraction χ are taken into account which is satisfactory.

4 Discussion

The key-issue deserving discussion concerns the treatment of elasticity in all previous atomic-scale simulation works on interfaces in Al/TiB_2 [20, 21] and other similar ternary systems (Al/SiO_2 [18], Mg/TiB_2 [19]). Surprisingly, these studies dismissed the methodology used in the simulation works of heterophase interfaces in binary systems [13, 14, 16, 39], in which this treatment was correctly performed. More precisely instead of ensuring convergence with the number of layers p, the authors in works [20,21] assumed that this convergence was guaranteed by sufficient numbers of layers in each of the Al and TiB_2 surfaces treated separately. However, this procedure, which amounts to selecting p arbitrarily, erroneously transfers conclusions deduced from homogeneous systems to heterogeneous ones and overlooks the coherency strain that induces in Al/TiB_2 a supplemental elastic energy absent from homogeneous structures [40, 41]. To illustrate clearly the influence of such arbitrary choice of p, Figure 11 displays the p dependence of Al/TiB_2 multilayer energies for FSC1 and FSC2 systems, redrawn from Figure 7 together with corresponding results for fixed p from previous works [20, 21]. It can be noted that, in the FSC2 case, the comparison is made more difficult by the fact that the p values are slightly different, $p = 19$ in work [21] whereas $p = 21$ in the present study, due to our correction to get identical interfaces absent from [21]. On the whole, Figure 11 clearly demonstrates that using arbitrary p values leads to strong overestimation of interface energies. Since similar remarks can be done for other interfaces such as Al/SiO_2 [18] and Mg/TiB_2 [19], this emphasizes the large ambiguity still existing on interface energies in these systems.

Another important issue is related to ambiguities inherent to simulations performed with FSC systems as done in earlier works [20, 21], due to the presence of strained surfaces in such systems, which may cast doubt on the relevant quantities to use in equations (9) and (10). Then, we propose in the following to investigate the effect of this deformation on the surface energies and subsequently, on the estimation of interface energies by means of FSC1 and FSC2 systems. During the interface atomic relaxation, both phases are deformed, but due to the strong discrepancy between Al and TiB_2 elastic constants, Al is more strained than TiB_2 as shown in Figure 10: a_{int} is closer to $a^{\text{eq}}_{TiB_2}$ than $a^{\text{eq}}_{\text{Al}}/\sqrt{2}$, which means that the coherency strain is mainly

accommodated by Al. Hence, only the effect of the deformation on the surface energy of Al is taken into account below. Applying equation (11), to obtain $\gamma^{\mathrm{Al}}_{(111)}$ for Al constrained in (111) plane, implies to know $E^{\mathrm{Al}}_{\mathrm{Ref}}$ for various levels of strain in the plane. For this purpose, $a^{\mathrm{Al}}_{(111)}$ is set at various values between the lattice parameter of non-deformed Al and TiB_2, i.e. $a^{\mathrm{eq}}_{\mathrm{Al}}/\sqrt{2}$ and $a^{\mathrm{eq}}_{\mathrm{TiB_2}}$. Then, for each of these values, the ab initio energies of the supercells with different lattice parameters along the direction perpendicular to the interface are calculated, the minimum energy yields $E^{\mathrm{Al}}_{\mathrm{Ref}}$ for a given value of $a^{\mathrm{Al}}_{(111)}$, as shown in Figure 12. Using the convergence criterion $p = 20$ for any lattice parameter $a^{\mathrm{Al}}_{(111)}$ (see Figure 3), the surface energy of strained Al $\gamma^{\mathrm{Al}}_{(111)}$ is then plotted as a function of $a^{\mathrm{Al}}_{(111)}$ (see Figure 13). The two limiting values are 0.693 $\mathrm{J/m^2}$ for non-deformed Al and 0.804 $\mathrm{J/m^2}$ for Al constrained by rigid TiB_2. Surprisingly, the surface energy displays a minimum and non-linear behavior with the in-plane lattice parameter. From Tables 3a and 3b, it was already seen noted that there are some significant differences between the interface energies estimated from FSC and PBC systems. The Al surface energy used to obtain these results was 0.693 $\mathrm{J/m^2}$ corresponding to non-deformed Al. Yet, from Figure 3, the Al surface energy depends on the in-plane lattice parameter. Tables C.1 and C.2, displaying the interfaces energies for each system calculated using the surface energy of strained Al, show that the Al surface energy has a significant influence on the interface energy, especially for FSC2, which should not be neglected, even if this impact is not sufficient to explain the gap between the FSC and PBC results. Then, the obtention of the surface energy to consider is far from being straightforward if we acknowledge deformed phases. Therefore, the derivation of the interface energies from FSC systems requires a delicate knowledge of surface energies for strained phases, which demonstrates that using PBC systems allows a more direct and more reliable estimation of interface energies in presence of coherency strain.

When discussing atomic-scale simulations of coherent heterophase interfaces, another point requiring close examination deals with the choice of criteria relevant to compare the relative stabilities of different interface configurations. In our work, we used interface energies as a stability criterion (labelled $\min(\sigma)$ below) to compare straightforwardly all configurations, the most stable configurations corresponding to lowest energies. In the previous studies dedicated to Al/TiB_2 interfaces [20, 21], an alternative strategy was employed to obtain the energies of the most stable interfaces, via a two-step procedure involving as an intermediate quantity the interface adhesion work W_{ad} and $\max(W_{\mathrm{ad}}(p,\chi))$ criterion. Whereas σ is a quantity intrinsic to a given interface configuration, $W_{\mathrm{ad}}(p,\chi)$ is a priori different for each multilayer with period p and TiB_2 proportion χ associated to the same configuration. Therefore, it is relevant first to check the equivalence of the $\min(\sigma)$ and $\max(W_{\mathrm{ad}}(p,\chi))$ criteria, when comparing interface configurations as regards stability. To this aim, equations (E.4) and (E.5) established in Appendix E and relating W_{ad} and σ are convenient. Using these equations, it should be noted that, provided the configurations compared have the same termination (Ti or B) of their TiB_2 side, the related surface energy term $\gamma^{\mathrm{TiB_2}}$ is equal for both configurations. Moreover, if p and χ are identical, then the elastic terms (see equations (E.4) and (E.5)) are also equal. This demonstrates that, under these conditions, the $\min(\sigma)$ and $\max(W_{\mathrm{ad}})$ indeed yield the same stability order for the couple of configurations studied. This justifies the first step of the procedure used in earlier works [20, 21], namely a $\max(W_{\mathrm{ad}})$-based classification among configurations with given TiB_2 termination. This lead the authors of works [20, 21] to the pre-selection (valid whatever the chemical potentials) of a couple (one Ti- and one B-terminated) of most favourable configurations, for which interface energies were then calculated explicitly in a second step. This is the reason why, in these previous studies [20, 21], interface energies were calculated for only two configurations (HCP Ti and HCP B), being respectively the most stable configurations with Ti and B terminations. While the foregoing arguments have confirmed the formal equivalence between both stability criteria, a second issue concerns the consistency of the results provided actually by these criteria in practical applications. To check this point, we performed a systematic comparison of both criteria for all

configurations of Al/TiB_2 basal interfaces (Tables E.1 and E.2) for both terminations and using FSC1 or FSC2 systems. As explained above, only adhesion works, not interface energies, were reported for all configurations in works [20, 21]. To allow comparison, our calculation are performed with the same numbers of layers p as in [20] (FSC1, $p = 12$,$\chi = 0.52$) and [21] (FSC2, $p = 19$,$\chi = 0.58$). The W_{ad} values are given in Tables E.1 and E.2 as well as the resulting order of interface stability. Confronting the two criteria $\min(\sigma)$ and $\max(W_{ad})$, the σ- and W_{ad}-deduced orders of stability are not the same for the Ti-terminated MT Ti, I3 and I2 configurations, in FSC1 as well as in FSC2 systems, which a priori contradicts the conclusion established above concerning the equivalence between both criteria. This contradiction can however be removed, recalling (see equations (E.4) and (E.5)) that these two criteria are expected to yield identical results only if the elastic energy density is strictly equal for the compared configurations, which is not the case according to Table 4. Since the σ values for these three configurations are close to each other, these small differences in the elastic energy density are sufficient to change the order of stability. Concerning configuration I1, there is a good agreement between both criteria, a high interface energy corresponding to a weak adhesion work. The same elasticity argument can be given to explain the stability inversions between both criteria for the B-terminated configurations. Comparing now these trends with earlier works, we have also reported in Tables E.1 and E.2 the adhesion works calculated in [20, 21]. Based on the $\min(\sigma)$ criterion, our work predicts, for Ti-terminated interfaces, that the I2, I3 and MT Ti configurations are the most favorable configurations, with interface energies close to each other. The same conclusions were reached in [20], reporting identical adhesion works (3.18 J/m^2) for these three configurations. However, the same work also reports for configuration I1 an adhesion work equal to 3.17 J/m^2, implying that I1 and the three aforemetioned configurations should be very similar in terms of W_{ad}, whereas σ values are very far apart in Table E.1. For the B-terminated configurations, the most stable configurations are MT B1 or I4 in our work, I4 in [20], and MT B2 and I5 in [21], so our work is in better agreement with [20]. Finally, it should also be noted that the W_{ad} values obtained in our work are quite different from those reported in [20,21] especially for Ti-terminated interfaces, whereas the numbers of layers used in each phase to perform the calculations are the same.

As mentioned previously, a last difficult issue with atomic-scale simulations of heterophase interfaces in chemically complex (non-binary) systems involving ordered compounds (TiB_2, SiO_2, Al/Mg_5Si_6) concerns the choice of the chemical potentials for the elements constituting these compounds. This choice has drastic consequences on interface energetics, and the chemical potentials were therefore kept as adjustable parameters in most earlier studies of these systems (Al/SiO_2 [18], Mg/TiB_2 [19], Al/TiB_2 [20, 21]), as well as in the current work on Al/TiB_2. However, in order to refine our picture of interfaces in such complex systems, it would be desirable to reach more accurate information on these important quantities. To this aim, considering specifically Al/TiB_2, it is useful to recall first that (i) the Ti and B chemical potentials are strongly dependent on the TiB_2 composition, undergoing steep variations at stoichiometry, and (ii) Ti and B chemical potentials characteristic of Ti excess in bulk TiB_2 also correspond preferentially to Ti-termination at TiB_2 surfaces and Al/TiB_2 interfaces. Keeping in mind these general features, the authors of recent ab initio studies of Al(L)/TiB_2 liquid-solid interfaces [22, 23] have attempted to infer some conclusions about relevant choices of TiB_2 composition and (Ti,B) chemical potentials. More precisely, the ab initio molecular dynamics simulations used in both of these works, revealed that local crystalline ordering of several Al(L) layers near the TiB_2 surface preferentially occurs for Ti-termination, a feature suggesting that this termination should possess a better nucleation power in the Al heterogeneous (i.e. on TiB_2 particles) solidification process. Similarly, another recent study of Al(L)/TiB_2 [42] relying of adsorption isotherms also led to conclude that the nucleation power of TiB_2 particles for solid Al should increase with Ti content. Although this conclusion can hardly be directly related to Ti and B chemical potentials (any absence of Ti terminations may not critically prevent solidification -

other kinds of preferential sites being possibly available to form Al solid nuclei), it is qualitatively in line with the experimental fact that Al-B-Ti master alloys (e.g. Al-5Ti-B) frequently have global Ti excess with respect to TiB_2 stoichiometry, suggesting that the same feature may hold for the TiB_2 compound. It should however be mentioned that TiB_2 particles are not always obtained from grain refiners: recent elaboration processes in 7075 Al alloys have rather involved in situ mixed salt method [2] inducing unknown TiB_2 composition. On the whole, this quick survey emphasizes that the handling of TiB_2 composition and (Ti,B) chemical potentials still currently remains quite intricate, leaving much room for further investigations. To make one step further in this direction, a possibility could be, still employing atomic-scale methods, to consider more thoroughly the thermodynamic equilibrium between TiB_2 particles and the surrounding Al-based alloy. This in turn may require investigating in detail TiB_2 properties, especially its point defect structure, via the independent-point-defect approximation (IPDA) [43], an approach already employed on various ordered compounds [43–47] as well as $MgZn_2$ [48] especially relevant in the context of Al-TiB_2 alloys.

To conclude this discussion, it should be pointed out that the present work was devoted only to basal interfaces in Al/TiB_2. However, other interfaces with different orientations (pyramidal, prismatic) are also involved between both phases. Due to the specific shape of TiB_2 particles [3], the study of prismatic interfaces would be of a special interest. However it was noted that the situation for such interfaces becomes so much more intricate than for basal ones. In the latter case, the whole study could be performed, in earlier works [20, 21] as in the present one, by assuming that these interfaces are fully coherent, which is a reasonable assumption since the mismatch in the TiB_2 basal plane remains moderate (6,45%). In prismatic interfaces, a first difficulty arises from the fact that according to the matching between Ti- and B- versus Al planes at the interface, two limiting kinds of coherent system can naturally be identified: (i) either Al planes are facing with Ti as well as B planes ($m = n$, m and n being respectively the number of planes in Al and TiB_2), (ii) or one Al planes are facing only with Ti planes, B planes being excluded from the correspondence ($n = m/2$). These two limiting cases lead to mismatch values in the interface plane (ϵ_{33}^{SFTS}) respectively equal to -26% and 45%. Due to these large values, prismatic interfaces can not be assumed coherent and a more realistic ratio of m/n must then be searched. One way to estimate it is to minimize the elastic energy, which consists in canceling the ϵ_{33}^{SFTS} component in the SFTS tensor: the expected theoretical ratio m/n is equal to 1.45 (see Appendix A.2). Thus, for investigations of prismatic interfaces using the same approach as for basal ones, supercells containing four $(111)_{Al}$ planes in correspondence with six $(0001)_{TiB_2}$ planes would be needed ($m/n = 3/2$). Provided the number of prismatic planes p is limited, this approach is still tractable. It turns out that this ratio is indeed the one obtained experimentally in [2,3], which confirms the validity of the method used in Appendix A.2 to calculate the SFTS tensor. Preliminary investigations suggest that simulations of prismatic interfaces may require significantly larger p values than for basal ones. However, this difficulty should not be critical, since the SFTS tensor established in Appendix A.2 could also be used in such cases to calculate the elastic energy using micro-elasticity theory for lower p values, thus allowing convenient extrapolation to cases beyond the capabilities of simulation.

5 Conclusion

Few theoretical works have been dedicated to coherent interfaces in non-binary systems, mainly due to thermodynamic and mechanical issues specific to them. Some available studies explore different chemical configurations at the interface, which requires to use the chemical potentials as control parameters varying on an interval for which the phases are expected to be stable. However, they ignore the coherency strain energy contribution in their methodology when deducing the interface energy. Other studies correctly handle elasticity but does not consider the possibility of different terminations at the interface. For the first time, this work fills the gap between these

two different approaches by optimizing the composition at the interface without overlooking the role of the elastic energy. More precisely, the coherency behavior of the heterogeneous systems is considered by extracting the elastic energy via a linear regression on multilayers by using first-principles calculations.

Our methodology offers significant improvements in the assessment of interfacial energies, as illustrated by the Al/TiB_2 basal interfaces for which a full set of nine configurations are analyzed. Like in the previous studies, the stability of Al/TiB_2 basal interfaces depends greatly on the chemical potentials in the TiB_2 phase, indeed in Ti-Rich (respectively B-Rich) conditions, Ti-terminated (respectively B-terminated) interfaces are the most favorable ones. However, the interface energies obtained are significantly different from previous results and suit more coherent interface energy level. This is partly due to the elastic contribution which is most of the time neglected in the literature, especially in non-binary systems. In order to rationalize the elastic results deduced from the ab initio calculations, they are compared to the elasticity theory and a good agreement is obtained, especially for PBC systems.

Some other methodological issues are investigated and among them the choice of the type of supercell used, either PBC or FSC. It appears that the use of FSC-type supercell requires the preliminary determination of surface energies. However, these surfaces are strained due to the coherency between both phases at the interface. It is shown in this paper that considering the energy of the strained surface instead of the energy of the stress-free surface can induce non-negligible changes of the resulting interface energy. The use of PBC-type supercells does not require such care and should be preferred for interface energy calculations with multilayers.

6 Acknowledgements

The authors are grateful to Dr Gang Ji for helpful discussions. They thank the Centre de Ressources Informatiques of the université de Lille (CRI) for computational facilities. Some of the figures in this work were generated using the VESTA software [29].

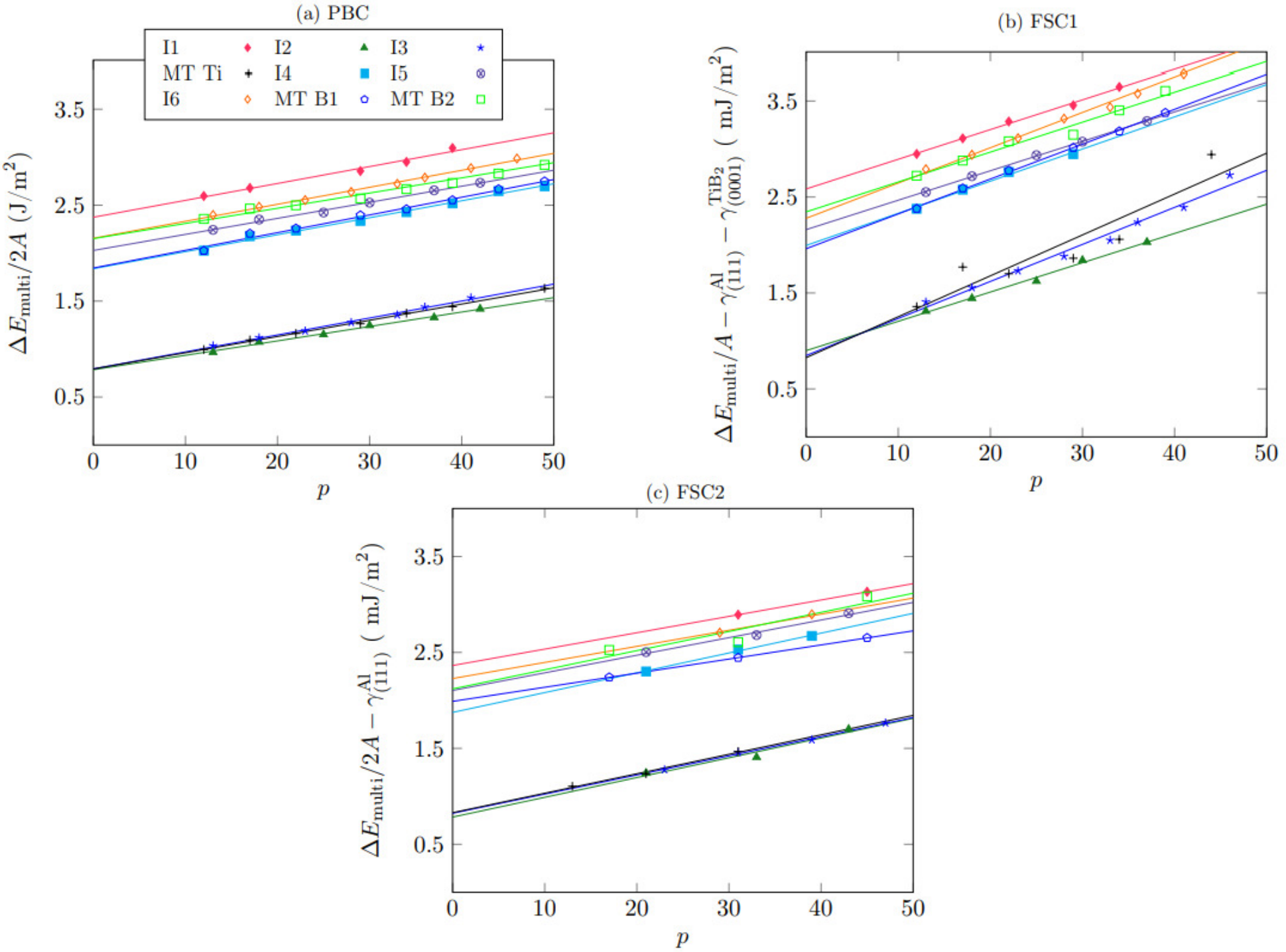

Figure 7. Ab initio energies of basal Al/TiB_2 multilayers for PBC, FSC1 and FSC2 systems in Ti-rich conditions ($\Delta\mu_{\text{Ti}} = -1.594\ eV$) as a function of the number of layers p (symbols). The lines refer to the linear regression performed to obtain interface energies. The TiB_2 volume fraction χ lies between 0.32 and 0.45 for PBC and FSC1 systems, and between 0.24 and 0.49 for FSC2 systems.

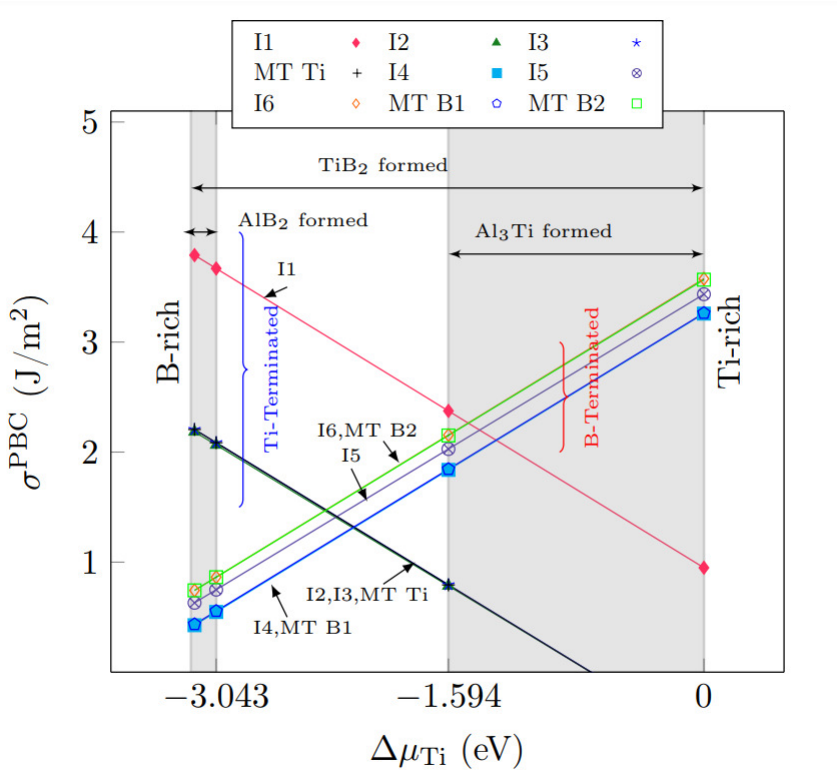

Figure 8. Interface energy of Al/TiB_2 basal interfaces as a function of $\Delta\mu_{Ti}$ for the nine configurations, in the case of PBC systems.

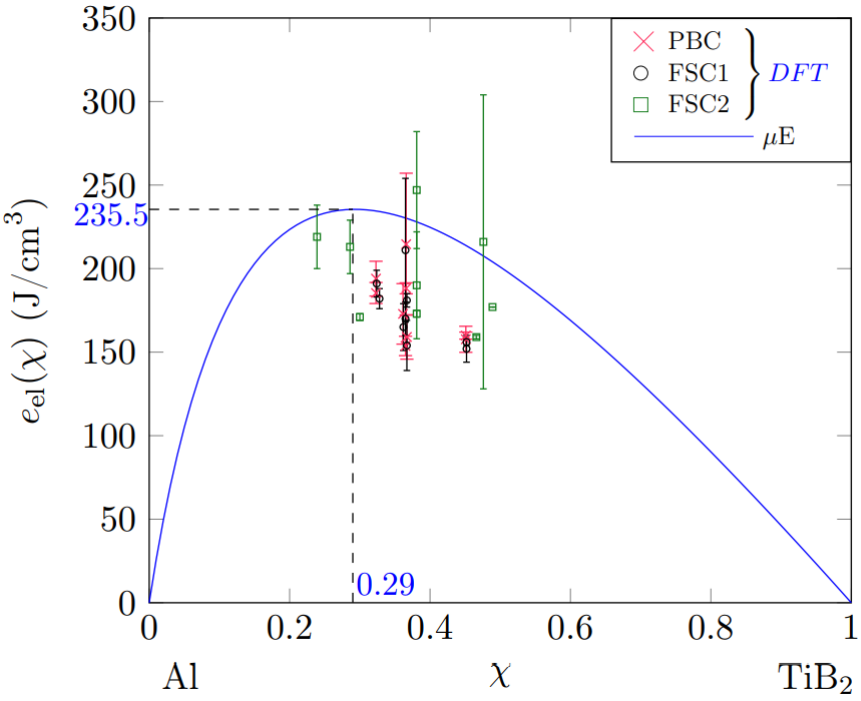

Figure 9. Elastic energy density of Al/TiB_2 basal interfaces as a function of the TiB_2 volume fraction χ obtained from DFT calculations (symbols) and micro-elasticity theory (line) with a maximum value of 235.5 J/cm^3 for χ=0.29. The vertical error bars are due to the linear regression and the surface energy. Another source of uncertainty is due to the χ quantity (Appendix D).

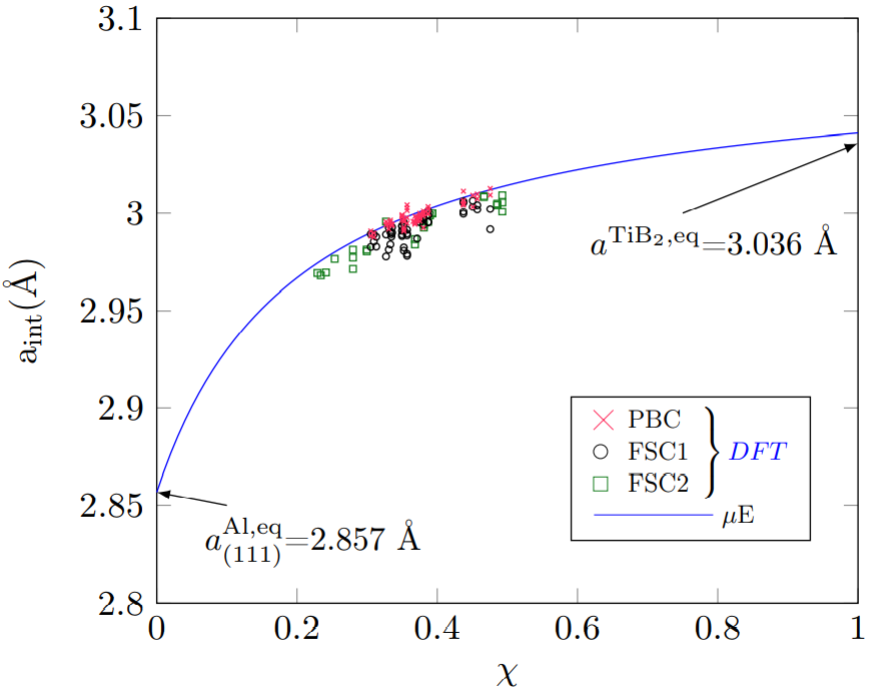

Figure 10. Common in-plane lattice parameter at the Al/TiB_2 basal interface obtained from μE theory (line) and from all the DFT calculations (symbols) for the various systems (PBC, FSC1 and FSC2) as a function of the TiB_2 volume fraction χ. Lattice parameters of non-deformed Al and TiB_2 are indicated in the graph.

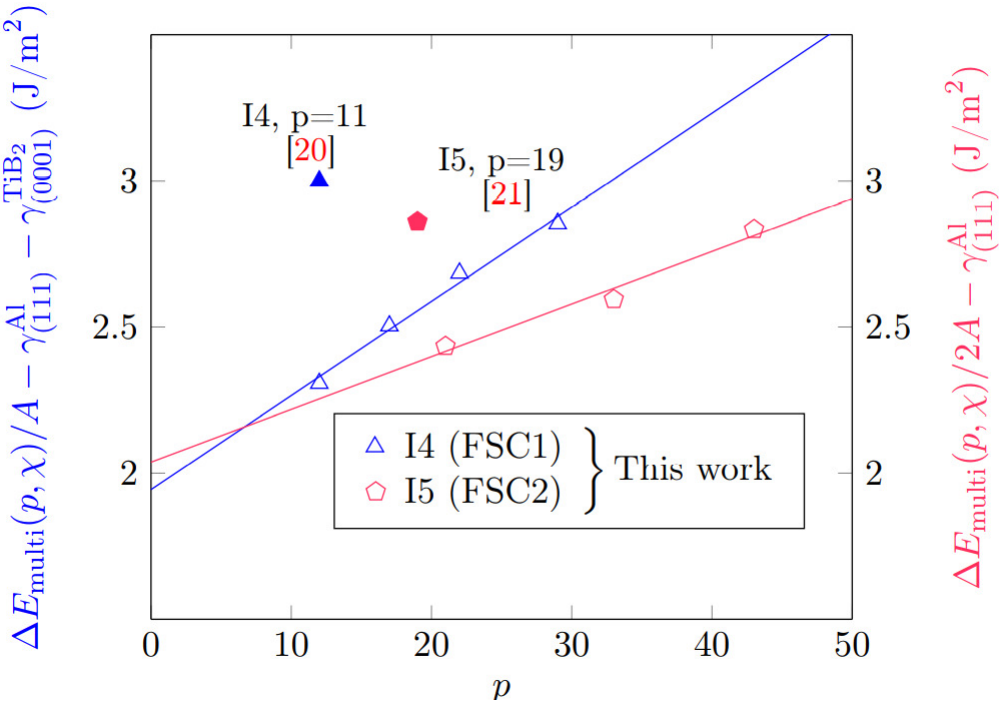

Figure 11. Multilayers energies of configuration I4 from FSC1 systems and configuration I5 from FSC2 systems in this work for $\Delta\mu_{\text{Ti}} = -1.594\ eV$. In addition values obtained from the literature [20, 21] for fixed p are also indicated in the graph for the same values of $\Delta\mu_{\text{Ti}}$.

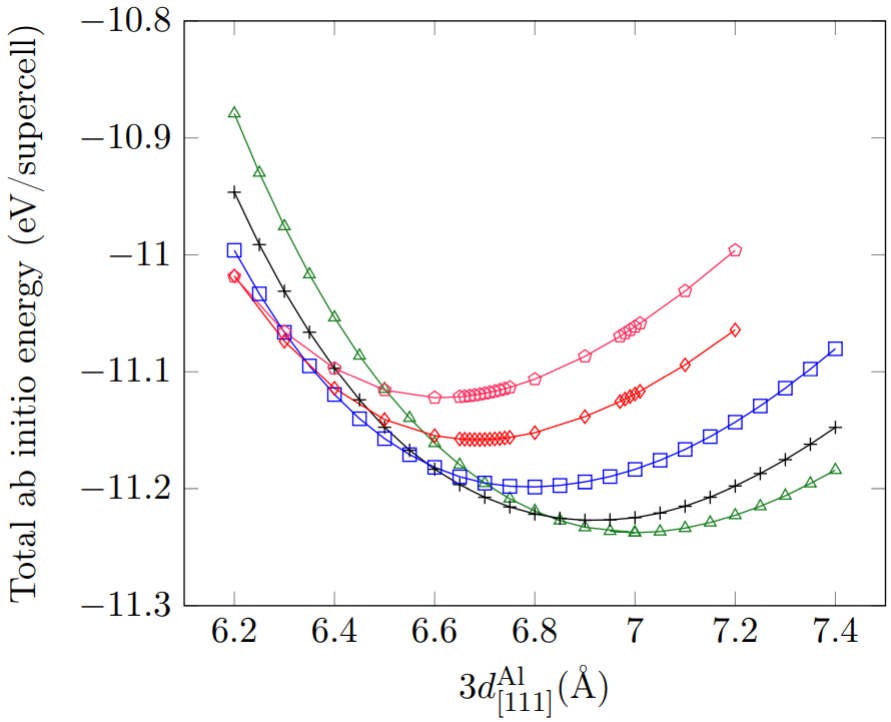

Figure 12. Total ab initio energy of deformed bulk Al as a function of the lattice parameter in the $[111]_{\mathrm{Al}}$ direction. The legend corresponding to the symbols is the same as on Figure 3.

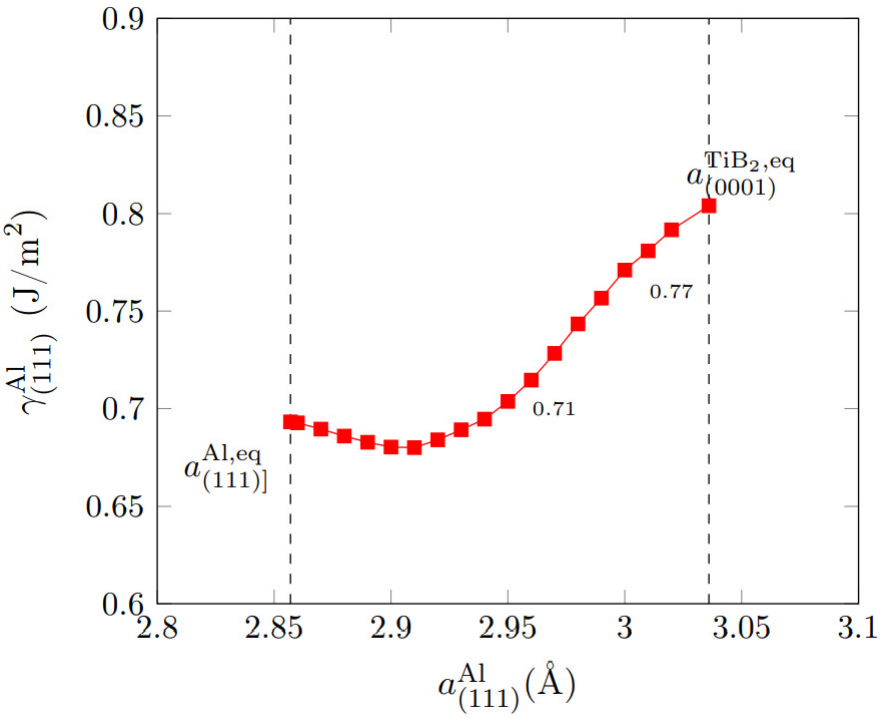

Figure 13. Surface energy of Al(111) slabs as a function of the lattice parameter $a^{\mathrm{Al}}_{(111)}$. The surface energy values are converged with the total number of layers p (Figure 3).

Appendices

A Elasticity of basal Al/TiB_2 interfaces

A.1 Bulk properties

Table A.1. Lattice parameters for both phases Al and TiB_2 (in Å).

		$a^{eq}_{TiB_2}$	$c^{eq}_{TiB_2}$	a^{eq}_{Al}
Theoretical	This work	3.036	3.232	4.0409
	[21]	3.035	3.226	4.047
	[20]	-	-	4.05
	[49]	3.029	3.220	-
Experimental	[30]	3.023-3.036	3.226-3.231	-
	[50]	3.033	3.231	-
	[51]	-	-	4.03
	[31]	-	-	4.04145

Table A.2. Elastic constants (in GPa) of Al from DFT calculations and comparison with the literature.

		C_{11}	C_{12}	C_{44}
Theoretical	This work	102	65	28
	[52]	104	60	28
Experimental	[53](300K)	107	61	28

Table A.3. Elastic constants (in GPa) of TiB_2 from DFT calculations and comparison with the literature.

		C_{11}	C_{12}	C_{13}	C_{33}	C_{44}	C_{66}
Theoretical	This work	637	71	102	437	253	283
	[54]	650	79	100	443	256	285
Experimental	[55]	660	48	93	432	260	306
	[56]	655	49	95	458	263	303

A.2 Stress free transformation strain (SFTS) tensor between Al and TiB_2

The preliminary determination of SFTS is essential to calculate the elastic energy of multilayered structures containing Al/TiB_2 interfaces. The general expression of the SFTS tensor is related to the matrix $\mathcal{F}$ of the Al→TiB_2 transformation by:

$$\epsilon^{SFTS} = \frac{\mathcal{F}^T.\mathcal{F} - \mathcal{I}}{2} \tag{A.1}$$

where I stands for the identity matrix and $\mathcal{F}^T$ is the transpose of $\mathcal{F}$. To get the matrix $\mathcal{F}$, three pairs of non-coplanar vectors, defined by the OR, are required:

$$\begin{cases} F(\frac{1}{2}[1\bar{1}0]_{\mathrm{Al}}) = \frac{1}{3}[11\bar{2}0]_{\mathrm{TiB_2}} \\ F(\frac{1}{2}[11\bar{2}]_{\mathrm{Al}}) = [\bar{1}100]_{\mathrm{TiB_2}} \\ F(n\frac{1}{3}[111]_{\mathrm{Al}}) = m\frac{1}{2}[0001]_{\mathrm{TiB_2}} \end{cases} \tag{A.2}$$

where we assume that n $(111)_{\mathrm{Al}}$ planes are in correspondence with m $(0001)_{\mathrm{TiB_2}}$ planes (m is the total number of Ti and B planes). Different definitions of a perfectly coherent prismatic interface can be proposed: one Al Plane is in correspondence with a Ti or a B plane ($m = n$), or one Al plane is in correspondence with one Ti plane only ($n = m/2$). However, experimentally, it is shown that prismatic interfaces are semi-coherent [2,3], which means that $n \neq m$ and $n \neq m/2$.

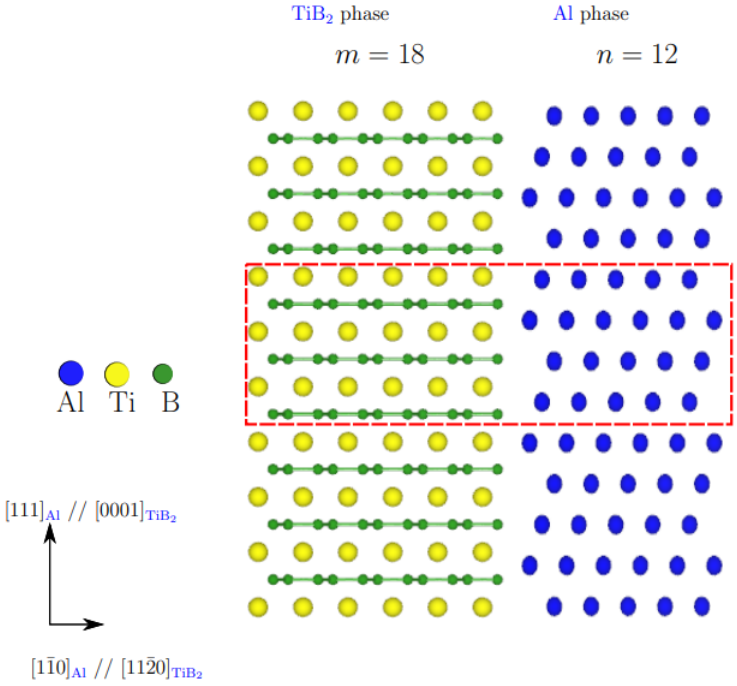

Figure A.1. Schematic representation of n $(111)_{\mathrm{Al}}$ planes and m $(0001)_{\mathrm{TiB_2}}$ planes in correspondence for a semi-coherent $\mathrm{Al/TiB_2}$ interface where m≠n. The dashed lines correspond to the semi-coherent interface supercell.

In the following all the calculations will be performed in the $\mathcal{R} = (\vec{x_1}, \vec{x_2}, \vec{x_3})$ basis (Figure 1). The non-coplanar vectors of (A.2) are expressed in this basis:

$$\begin{cases} \frac{1}{2}[1\bar{1}0]_{\mathrm{Al}} = \frac{a^{\mathrm{eq}}_{\mathrm{Al}}}{\sqrt{2}}\vec{x_1} \\ \frac{1}{2}[11\bar{2}]_{\mathrm{Al}} = \sqrt{3}(\frac{a^{\mathrm{eq}}_{\mathrm{Al}}}{\sqrt{2}})\vec{x_2} \\ \frac{1}{3}[111]_{\mathrm{Al}} = d^{\mathrm{eq}}_{\mathrm{Al}[111]}\vec{x_3} \end{cases} \tag{A.3}$$

with $d^{\mathrm{eq}}_{\mathrm{Al}[111]} = \frac{a^{\mathrm{eq}}_{\mathrm{Al}}}{\sqrt{3}}$ and,

$$\begin{cases} \frac{1}{3}[11\bar{2}0]_{\mathrm{TiB_2}} = a^{\mathrm{eq}}_{\mathrm{TiB_2}}\vec{x_1} \\ [\bar{1}100]_{\mathrm{TiB_2}} = \sqrt{3}a^{\mathrm{eq}}_{\mathrm{TiB_2}}\vec{x_2} \\ [0001]_{\mathrm{TiB_2}} = c^{\mathrm{eq}}_{\mathrm{TiB_2}}\vec{x_3} \end{cases} \tag{A.4}$$

The matrix $\mathcal{F}$ can then be deduced from:

$$F.\begin{pmatrix} \frac{a^{eq}_{Al}}{\sqrt{2}} & 0 & 0 \\ 0 & \sqrt{3}(\frac{a^{eq}_{Al}}{\sqrt{2}}) & 0 \\ 0 & 0 & d^{eq}_{Al[111]} \end{pmatrix} = \begin{pmatrix} a^{eq}_{TiB_2} & 0 & 0 \\ 0 & \sqrt{3}a^{eq}_{TiB_2} & 0 \\ 0 & 0 & \frac{m}{n}\frac{1}{2}c^{eq}_{TiB_2} \end{pmatrix} \tag{A.5}$$

it follows that:

$$F = \begin{bmatrix} \sqrt{2}(\frac{a^{eq}_{TiB_2}}{a^{eq}_{Al}}) & 0 & 0 \\ 0 & \sqrt{2}(\frac{a^{eq}_{TiB_2}}{a^{eq}_{Al}}) & 0 \\ 0 & 0 & \frac{1}{2}\frac{m}{n}\frac{c^{eq}_{TiB_2}}{d^{eq}_{Al[111]}} \end{bmatrix}_{\mathcal{R}} \tag{A.6}$$

and from (A.1):

$$\epsilon^{SFTS} = \begin{bmatrix} (\frac{a^{eq}_{TiB_2}}{a^{eq}_{Al}})^2 - \frac{1}{2} & 0 & 0 \\ 0 & (\frac{a^{eq}_{TiB_2}}{a^{eq}_{Al}})^2 & 0 \\ 0 & 0 & \frac{1}{2}((\frac{1}{2}\frac{m}{n}\frac{c^{eq}_{TiB_2}}{d^{eq}_{Al[111]}})^2 - 1) \end{bmatrix}_{\mathcal{R}} \tag{A.7}$$

By reporting in equation (A.7) the values of the lattice parameters of both Al and TiB_2 calculated in this work (Table A.1), we obtain ϵ^{SFTS}_{11}=ϵ^{SFTS}_{22}=6.447%. The value of the ratio m/n can be estimated by assuming it cancels ϵ^{SFTS}_{33} in order to minimize the elastic energy:

$\frac{1}{2}((\frac{1}{2}\frac{m}{n}\frac{c^{eq}_{TiB_2}}{d^{eq}_{Al[111]}})^2 - 1) = 0 \Rightarrow \frac{m}{n} = \frac{2d^{eq}_{Al[111]}}{c^{eq}_{TiB_2}} \approx 1.45$

Under the constraint that m must be even by definition, the smallest values of m and n fulfilling this condition is $m = 6$ and $n = 4$ (4 Al planes in correspondence with 3 Ti and 3 B planes). This ratio is indeed the one obtained experimentally [2, 3].

A.3 Elastic energy density e_{el}

In the following ϵ^{ϕ} is the elastic strain tensor of phase ϕ in epitaxial relation with the other phase. Due to the symmetrical properties of Al and TiB_2, it can be shown that ϵ^{ϕ} has the following form in $\mathcal{R}$ when a basal interface is present between both phases:

$$\epsilon^{\phi} = \begin{bmatrix} \epsilon^{\phi}_{11} & 0 & 0 \\ 0 & \epsilon^{\phi}_{11} & 0 \\ 0 & 0 & \epsilon^{\phi}_{33} \end{bmatrix}_{\mathcal{R}} \quad \text{with } \phi = \text{Al or } TiB_2 \tag{A.8}$$

The epitaxial relation at the interface $(\vec{x_1}, \vec{x_2})$ implies:

$$\epsilon^{Al}_{ii} = \epsilon^{SFTS}_{ii} + \epsilon^{TiB_2}_{ii} \text{ with i=1,2} \tag{A.9}$$

Elastic energy density e^{ϕ}_{el} of phase ϕ is defined as:

$$e^{\phi}_{el} = \frac{1}{2}c^{\phi}_{ijkl}\epsilon^{\phi}_{ij}\epsilon^{\phi}_{kl} \tag{A.10}$$

where c^{ϕ}_{ijkl} are the elastic constants of phase ϕ. Al phase belongs to crystallographic group F m -3 m. Due to the cubic symmetry, the tensor of the elastic constants can be written as follows:

$$C^{c,\mathrm{Al}} = \begin{bmatrix} C_{11}^{c,\mathrm{Al}} & C_{12}^{c,\mathrm{Al}} & C_{12}^{c,\mathrm{Al}} & 0 & 0 & 0 \\ C_{12}^{c,\mathrm{Al}} & C_{11}^{c,\mathrm{Al}} & C_{12}^{c,\mathrm{Al}} & 0 & 0 & 0 \\ C_{12}^{c,\mathrm{Al}} & C_{12}^{c,\mathrm{Al}} & C_{11}^{c,\mathrm{Al}} & 0 & 0 & 0 \\ 0 & 0 & 0 & C_{44}^{c,\mathrm{Al}} & 0 & 0 \\ 0 & 0 & 0 & 0 & C_{44}^{c,\mathrm{Al}} & 0 \\ 0 & 0 & 0 & 0 & 0 & C_{44}^{c,\mathrm{Al}} \end{bmatrix}_{\mathcal{R}^c} \tag{A.11}$$

where $\mathcal{R}^c = (\vec{a_1}, \vec{a_2}, \vec{a_3})$ with $\vec{a_1}//[100], \vec{a_2}//[010], \vec{a_3}//[001]$. Since all the calculations are made in $\mathcal{R}$ this tensor must be expressed in the same basis. Through a change of bases ($\mathcal{R}^c \to \mathcal{R}$) it can be shown that:

$$C^{\mathrm{Al}} = \begin{bmatrix} C_{11}^{\mathrm{Al}} & C_{12}^{\mathrm{Al}} & C_{13}^{\mathrm{Al}} & C_{14}^{\mathrm{Al}} & 0 & 0 \\ C_{12}^{\mathrm{Al}} & C_{11}^{\mathrm{Al}} & C_{13}^{\mathrm{Al}} & -C_{14}^{\mathrm{Al}} & 0 & 0 \\ C_{13}^{\mathrm{Al}} & C_{13}^{\mathrm{Al}} & C_{33}^{\mathrm{Al}} & 0 & 0 & 0 \\ C_{14}^{\mathrm{Al}} & -C_{14}^{\mathrm{Al}} & 0 & C_{44}^{\mathrm{Al}} & 0 & 0 \\ 0 & 0 & 0 & 0 & C_{44}^{\mathrm{Al}} & C_{14}^{\mathrm{Al}} \\ 0 & 0 & 0 & 0 & C_{14}^{\mathrm{Al}} & C_{66}^{\mathrm{Al}} \end{bmatrix}_{\mathcal{R}} \tag{A.12}$$

$$\text{with} \begin{cases} C_{11}^{\mathrm{Al}} = \frac{1}{2}(C_{11}^{c,\mathrm{Al}} + C_{12}^{c,\mathrm{Al}} + 2C_{44}^{c,\mathrm{Al}}) \\ C_{12}^{\mathrm{Al}} = \frac{1}{6}(C_{11}^{c,\mathrm{Al}} + 5C_{12}^{c,\mathrm{Al}} - 2C_{44}^{c,\mathrm{Al}}) \\ C_{13}^{\mathrm{Al}} = \frac{1}{3}(C_{11}^{c,\mathrm{Al}} + 2C_{12}^{c,\mathrm{Al}} - 2C_{44}^{c,\mathrm{Al}}) \\ C_{33}^{\mathrm{Al}} = \frac{1}{3}(C_{11}^{c,\mathrm{Al}} + 2C_{12}^{c,\mathrm{Al}} + 4C_{44}^{c,\mathrm{Al}}) \\ C_{14}^{\mathrm{Al}} = \frac{C_{11}^{c,\mathrm{Al}} - C_{12}^{c,\mathrm{Al}} - 2C_{44}^{c,\mathrm{Al}}}{3\sqrt{2}} \\ C_{44}^{\mathrm{Al}} = \frac{1}{3}(C_{11}^{c,\mathrm{Al}} - C_{12}^{c,\mathrm{Al}} + C_{44}^{c,\mathrm{Al}}) \\ C_{66}^{\mathrm{Al}} = \frac{1}{6}(C_{11}^{c,\mathrm{Al}} - C_{12}^{c,\mathrm{Al}} + 4C_{44}^{c,\mathrm{Al}}) \end{cases} \tag{A.13}$$

From (A.10), it follows that:

$$\begin{aligned} 2e_{\mathrm{el}}^{\mathrm{Al}} = C_{11}^{\mathrm{Al}}((\epsilon_{11}^{\mathrm{Al}})^2 + (\epsilon_{22}^{\mathrm{Al}})^2) + 2C_{12}^{\mathrm{Al}}\epsilon_{22}^{\mathrm{Al}}\epsilon_{11}^{\mathrm{Al}} + C_{13}^{\mathrm{Al}}(2\epsilon_{33}^{\mathrm{Al}}\epsilon_{11}^{\mathrm{Al}} + 2\epsilon_{33}^{\mathrm{Al}}\epsilon_{22}^{\mathrm{Al}}) + C_{33}^{\mathrm{Al}}(\epsilon_{33}^{\mathrm{Al}})^2 + \\ C_{14}^{\mathrm{Al}}(4\epsilon_{23}^{\mathrm{Al}}\epsilon_{11}^{\mathrm{Al}} - 4\epsilon_{23}^{\mathrm{Al}}\epsilon_{22}^{\mathrm{Al}} + 4\epsilon_{12}^{\mathrm{Al}}\epsilon_{31}^{\mathrm{Al}}) + C_{44}^{\mathrm{Al}}(4(\epsilon_{23}^{\mathrm{Al}})^2 + 4(\epsilon_{31}^{\mathrm{Al}})^2) + 4C_{66}^{\mathrm{Al}}(\epsilon_{12}^{\mathrm{Al}})^2 \end{aligned} \tag{A.14}$$

According to (A.8), $\epsilon_{11}^{\mathrm{Al}} = \epsilon_{22}^{\mathrm{Al}}$ and $\epsilon_{ij}^{\mathrm{Al}} = 0$ if $i \neq j$. Therefore (A.14) becomes:

$$e_{\mathrm{el}}^{\mathrm{Al}} = (C_{11}^{\mathrm{Al}} + C_{12}^{\mathrm{Al}})(\epsilon_{11}^{\mathrm{Al}})^2 + 2C_{13}^{\mathrm{Al}}\epsilon_{11}^{\mathrm{Al}}\epsilon_{33}^{\mathrm{Al}} + \frac{1}{2}C_{33}^{\mathrm{Al}}(\epsilon_{33}^{\mathrm{Al}})^2 \tag{A.15}$$

Phase TiB_2 belongs to crystallographic space group P6/mmm and possesses an hexagonal symmetry. The elastic constants tensor can be written as a function of 5 elastic constants and has the same form as (A.12) in $\mathcal{R}$ with $C_{14}^{\mathrm{TiB_2}} = 0$, $C_{66}^{\mathrm{TiB_2}} = \frac{1}{2}(C_{11}^{\mathrm{TiB_2}} - C_{12}^{\mathrm{TiB_2}})$, therefore:

$$e_{\mathrm{el}}^{\mathrm{TiB_2}} = (C_{11}^{\mathrm{TiB_2}} + C_{12}^{\mathrm{TiB_2}})(\epsilon_{11}^{\mathrm{TiB_2}})^2 + 2C_{13}^{\mathrm{TiB_2}}\epsilon_{11}^{\mathrm{TiB_2}}\epsilon_{33}^{\mathrm{TiB_2}} + \frac{1}{2}C_{33}^{\mathrm{TiB_2}}(\epsilon_{33}^{\mathrm{TiB_2}})^2 \tag{A.16}$$

At this stage in order to calculate e_{el}^{ϕ} given by (A.15) and (A.16), we need to calculate ϵ_{11}^{ϕ} and ϵ_{33}^{ϕ} in each phase ϕ. For this purpose, a two-step procedure is applied. First, in each phase ϕ, for a given value of ϵ_{11}^{ϕ}, we determine ϵ_{33}^{ϕ} which minimizes e_{el}^{ϕ}:

$$\frac{\partial e_{\text{el}}^{\phi}}{\partial \epsilon_{33}^{\phi}} = 0 \Rightarrow 2C_{13}^{\phi}\epsilon_{11}^{\phi} + C_{33}^{\phi}\epsilon_{33}^{\phi} = 0$$
$$\Rightarrow \epsilon_{33}^{\phi} = -\frac{2C_{13}^{\phi}}{C_{33}^{\phi}}\epsilon_{11}^{\phi} \tag{A.17}$$

by reporting (A.17) in (A.15) and (A.16) e_{el}^{ϕ} can be expressed as:

$$e_{\text{el}}^{\phi} = \text{A}^{\phi}(\epsilon_{11}^{\phi})^2 \text{ with } \text{A}^{\phi} = C_{11}^{\phi} + C_{12}^{\phi} - 2\frac{C_{13}^{\phi}.C_{13}^{\phi}}{C_{33}^{\phi}} \tag{A.18}$$

If V_{Al} and V_{TiB_2} are respectively the volumes of the Al and TiB_2 phases, the total elastic energy of the multilayer is $V_{\text{Al}}A^{\text{Al}}{\epsilon_{11}^{\text{Al}}}^2 + V_{\text{TiB}_2}A^{\text{TiB}_2}{\epsilon_{11}^{\text{TiB}_2}}^2$. The associated elastic energy density is then is:

$$\begin{aligned} e_{\text{el}} &= \frac{V_{\text{Al}}A^{\text{Al}}(\epsilon_{11}^{\text{Al}})^2 + V_{\text{TiB}_2}A^{\text{TiB}_2}(\epsilon_{11}^{\text{TiB}_2})^2}{V_{\text{Al}} + V_{\text{TiB}_2}} \\ &= (1-\chi)A^{\text{Al}}(\epsilon_{11}^{\text{Al}})^2 + \chi A^{\text{TiB}_2}(\epsilon_{11}^{\text{TiB}_2})^2 \\ &= (1-\chi)A^{\text{Al}}(\epsilon_{11}^{\text{Al}})^2 + \chi A^{\text{TiB}_2}(\epsilon_{11}^{\text{Al}} - \epsilon_{11}^{SFTS})^2 \end{aligned} \tag{A.19}$$

with $\chi = \frac{V_{\text{TiB}_2}}{V_{\text{Al}}+V_{\text{TiB}_2}}$. In a second step, $\epsilon_{11}^{\text{Al}}$ is determined by minimizing e_{el}:

$$\frac{\partial e_{\text{el}}}{\partial \epsilon_{11}^{\text{Al}}} = 0 \Rightarrow \epsilon_{11}^{\text{Al}} = \frac{\chi A^{\text{TiB}_2}\epsilon_{11}^{SFTS}}{\chi A^{\text{TiB}_2} + (1-\chi)A^{\text{Al}}} \tag{A.20}$$

by reporting equation (A.20) in equation (A.19), we obtain a new expression of the elastic energy density only as a function of χ, the elastic constants of Al and TiB_2, and ϵ_{11}^{SFTS}:

$$e_{\text{el}} = \frac{\chi(1-\chi)A^{\text{TiB}_2}A^{\text{Al}}(\epsilon_{11}^{SFTS})^2}{\chi A^{\text{TiB}_2} + (1-\chi)A^{\text{Al}}} \tag{A.21}$$

A.4 Determination of the interface lattice parameter

In order to get the lattice parameter of the Al/TiB_2 interface a_{int}, the relationship between a_{Al} and the elastic strain $\epsilon_{11}^{\text{Al}}$ must be obtained. To do so, we determine the strain tensor for the deformation of Al $\text{Al}^{\text{FCC}} \rightarrow \text{Al}^{\text{deformed}}$ with the following non-coplanar vectors:

$$\begin{cases} F(\frac{1}{2}[1\bar{1}0]_{\text{Al}}) = \frac{1}{2}[1\bar{1}0]_{\text{Al}}^{\text{deformed}} \\ F(\frac{1}{2}[11\bar{2}]_{\text{Al}}) = \frac{1}{2}[11\bar{2}]_{\text{Al}}^{\text{deformed}} \\ F(\frac{1}{3}[111]_{\text{Al}}) = \frac{1}{3}[111]_{\text{Al}}^{\text{deformed}} \end{cases} \tag{A.22}$$

those vectors can be written in $\mathcal{R}$:

$$\begin{cases} \frac{1}{2}[1\bar{1}0]_{\text{Al}} = \frac{a_{\text{Al}}^{\text{eq}}}{\sqrt{2}}\vec{x_1} \\ \frac{1}{2}[11\bar{2}]_{\text{Al}} = \sqrt{3}(\frac{a_{\text{Al}}^{\text{eq}}}{\sqrt{2}})\vec{x_2} \\ \frac{1}{3}[111]_{\text{Al}} = d_{\text{Al}[111]}^{\text{eq}}\vec{x_3} \end{cases} \tag{A.23}$$

$$\begin{cases} \frac{1}{2}[1\bar{1}0]^{\text{deformed}}_{\text{Al}} = \frac{a^{\text{deformed}}_{\text{Al}}}{\sqrt{2}}\vec{x_1} \\ \frac{1}{2}[11\bar{2}]^{\text{deformed}}_{\text{Al}} = \sqrt{3}(\frac{a^{\text{deformed}}_{\text{Al}}}{\sqrt{2}})\vec{x_2} \\ \frac{1}{3}[111]^{\text{deformed}}_{\text{Al}} = d^{\text{deformed}}_{\text{Al}[111]}\vec{x_3} \end{cases} \tag{A.24}$$

from (A.22) and with $a_{\text{int}} = \frac{a^{\text{deformed}}_{\text{Al}}}{\sqrt{2}}$:

$$F = \begin{bmatrix} \frac{a_{\text{int}}}{a^{\text{eq}}_{\text{Al}}}\sqrt{2} & 0 & 0 \\ 0 & \frac{a_{\text{int}}}{a^{\text{eq}}_{\text{Al}}}\sqrt{2} & 0 \\ 0 & 0 & \frac{d^{\text{deformed}}_{\text{Al}[111]}}{d^{\text{eq}}_{\text{Al}[111]}} \end{bmatrix}_{\mathcal{R}} \tag{A.25}$$

and from (A.1):

$$\epsilon^{\text{Al}} = \begin{bmatrix} \frac{1}{2}\frac{a^2_{\text{int}}}{(\frac{a^{\text{eq}}_{\text{Al}}}{\sqrt{2}})^2} - \frac{1}{2} & 0 & 0 \\ 0 & \frac{1}{2}\frac{a^2_{\text{int}}}{(\frac{a^{\text{eq}}_{\text{Al}}}{\sqrt{2}})^2} - \frac{1}{2} & 0 \\ 0 & 0 & \frac{1}{2}(\frac{d^{\text{deformed}}_{\text{Al}[111]}}{d^{\text{eq}}_{\text{Al}[111]}})^2 - \frac{1}{2} \end{bmatrix}_{\mathcal{R}} \tag{A.26}$$

therefore:

$$a_{\text{int}} = \frac{a^{\text{eq}}_{\text{Al}}}{\sqrt{2}}\sqrt{(2\epsilon^{\text{Al}}_{11} + 1)} \tag{A.27}$$

$\epsilon^{\text{Al}}_{11}$ being given by (A.20).

B Chemical potentials in Al-Ti-B systems

To calculate ΔE_{multi} in the previous equations (8), (9) and (10), chemical potentials of each species are needed beforehand. The main difficulty consists in determining Ti and B chemical potentials in the TiB_2 phase. Because these quantities are unknown, the approach that overcomes this issue is to use a chemical potential range of interest in which TiB_2 exists as in previous studies [20, 21, 32, 57]. However, some uncertainties remain on the methodology used in [20, 21] and the present work aims at bringing some clarifications. Indeed, from the reactions that lead to the formation of TiB_2 from Al-Ti-B system, other phases can potentially form such as Al_3Ti and AlB_2. Moreover, those former phases are not identified in the work of Ma et al. [2, 3] which emphasizes the necessity to avoid the formation of Al_3Ti and AlB_2 phases in the present work.

Avoiding $\alpha - \text{Ti}$ and $\alpha - \text{B12}$ formation from TiB_2

Figure B.1 represents the free energies of $\alpha - \text{Ti}$ and TiB_2 phases as a function of the composition of B in the binary Ti-B system. TiB_2 and $\alpha - \text{Ti}$ phases are in thermodynamic equilibrium for a composition x_{eq} ($\approx 2/3$) of TiB_2. For $x_1 \leq x_{\text{eq}}$, the free energy of the TiB_2 phase G_1 ($=G_{TiB_2}(x_1)$ on Figure B.1) would be greater than the free energy G_2 (given by the common tangent) of the biphasic system TiB_2 $+\alpha$-Ti at their equilibrium compositions, making more favorable the formation of $\alpha - \text{Ti}$ from the TiB_2 phase. Therefore, to avoid $\alpha - \text{Ti}$ formation, the condition $G_1 \leq G_2$ must be fulfilled, resulting in $x_1 \geq x_{\text{eq}}$ and $\mu_{\text{Ti}}^{\text{TiB}_2} \leq \mu_{\text{Ti}}^{\text{TiB}_2 \rightleftharpoons \alpha-\text{Ti}}$, where $\mu_{\text{Ti}}^{\text{TiB}_2 \rightleftharpoons \alpha-\text{Ti}}$ is the chemical potential of Ti in TiB_2 in equilibrium with α-Ti ($\approx E_{\text{Ref}}^{\alpha\text{-Ti}}$). In the same way, from Figure B.2, for a composition $x_2 \geq x_{\text{eq}}$, the free energy of the TiB_2 phase G_3 ($G_{TiB_2}(x_2)$) would be greater than the free energy G_4 of the biphasic system TiB_2 $+\alpha$-B12 at equilibrium, promoting the formation of $\alpha - \text{B12}$ from the TiB_2 phase. To overcome this, $G_3 \leq G_4$ which leads to $H_f(TiB_2) + E_{\text{Ref}}^{\alpha\text{-Ti}} \leq \mu_{\text{Ti}}^{\text{TiB}_2}$. Hence, the condition to avoid $\alpha - \text{Ti}$ and $\alpha - \text{B12}$ formation at the expense of TiB_2 is given by the following inequality:

$$H_f(TiB_2) \leq \mu_{\text{Ti}}^{\text{TiB}_2} - E_{\text{Ref}}^{\alpha\text{-Ti}} \leq 0 \tag{B.1}$$

Avoiding Al_3Ti formation from TiB_2

Figure B.3 represents the free energies of Al and Al_3Ti phases as a function of the composition of Ti in the binary Al-Ti system. The thermodynamic equilibrium between Al and Al_3Ti phases is reached for a Ti composition in Al_3Ti noted x_{eq} (≈ 0.25). If the chemical potential of Ti in TiB_2 is greater than the chemical potential of Ti in Al_3Ti in equilibrium with Al noted $\mu_{\text{Ti}}^{\text{Al}_3\text{Ti} \rightleftharpoons \text{Al}}$, then there will be a thermodynamic driving force to form the Al_3Ti phase from the Al and TiB_2 phases. From Figure B.3, it is easy to demonstrate that $\mu_{\text{Ti}}^{\text{Al}_3\text{Ti} \rightleftharpoons \text{Al}} = H_f(Al_3Ti) + E_{\text{Ref}}^{\alpha\text{-Ti}}$. Thus the condition to avoid the formation of Al_3Ti phase from TiB_2 phase is:

$$\mu_{\text{Ti}}^{\text{TiB}_2} - E_{\text{Ref}}^{\alpha\text{-Ti}} \leq H_f(Al_3Ti) \tag{B.2}$$

Avoiding AlB_2 formation from TiB_2

Figure B.4 represents the free energies of Al and AlB_2 phases in the binary Al-B system as a function of the B composition. The composition of the AlB_2 phase in equilibrium with Al is noted x_{eq} in Figure B.4 ($\approx 2/3$). To prevent the formation of AlB_2, $\mu_{\text{B}}^{\text{TiB}_2} \leq \mu_{\text{B}}^{\text{Al} \rightleftharpoons \text{AlB}_2}$, where $\mu_{\text{B}}^{\text{Al} \rightleftharpoons \text{AlB}_2}$ is the chemical potential of B in AlB_2 in equilibrium with Al. From Figure B.4a), $\mu_{\text{B}}^{\text{Al} \rightleftharpoons \text{AlB}_2} = \frac{1}{2} H_f(AlB_2) + E_{\text{Ref}}^{\alpha\text{-B12}}$. From Figure B.4b), this inequality is also equivalent to $\mu_{\text{Ti}}^{\text{TiB}_2} \geq H_f(AlB_2) + E_{\text{Ref}}^{\alpha\text{-Ti}} + H_f(TiB_2)$. Lastly, avoiding the formation of AlB_2 phase leads to the following inequality:

$$H_f(TiB_2) - H_f(AlB_2) \leq \mu_{\text{Ti}}^{\text{TiB}_2} - E_{\text{Ref}}^{\alpha\text{-Ti}} \tag{B.3}$$

Finally, the range of interest leading to the existence of TiB_2 without the formation of any other phases is :

$$H_f(TiB_2) - H_f(AlB_2) \leq \mu_{Ti}^{TiB_2} - E_{Ref}^{\alpha\text{-}Ti} \leq H_f(Al_3Ti) \tag{B.4}$$

and numerically:

$$-3.043eV \leq \mu_{Ti}^{TiB_2} - E_{Ref}^{\alpha\text{-}Ti} \leq -1.594eV \tag{B.5}$$

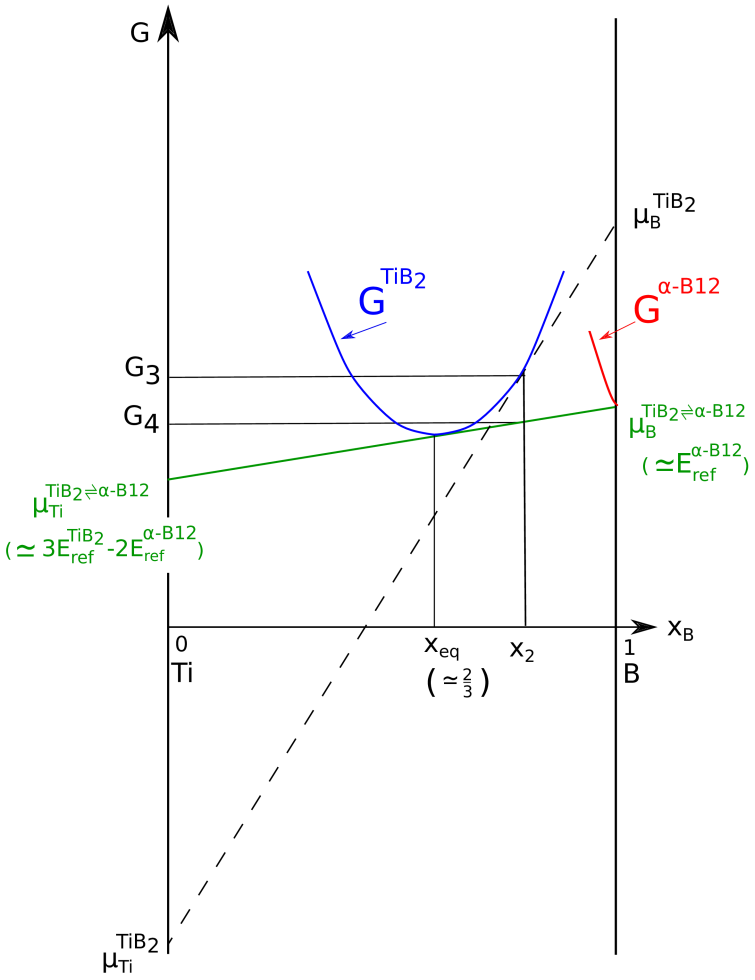

Figure B.1. Gibbs free energies G (in eV/atom) of α-Ti and TiB_2 phases as a function of the boron composition in the Ti-B system. The green line stands for the common tangent. Its intersections with the axes $x_B = 0$ and $x_B = 1$ give respectively the equilibrium chemical potentials of Ti and B noted $\mu_{Ti}^{TiB_2 \rightleftharpoons \alpha-Ti}$ and $\mu_B^{TiB_2 \rightleftharpoons \alpha-Ti}$. The Gibbs free energy of TiB_2 at composition x_1 is noted G_1. For the same composition, the common tangent gives the Gibbs free energy G_2 of the mixture of α-Ti and TiB_2 at equilibrium. Since $G_2 < G_1$, the formation of α-Ti from TiB_2 is promoted. the dotted line stands for the tangent to G_{TiB_2} at composition x_1. Its intersections with the axes $x_B = 0$ and $x_B = 1$ give respectively the chemical potentials $\mu_{Ti}^{TiB_2}$ and $\mu_B^{TiB_2}$ in TiB_2 at this composition. It can be seen that $\mu_{Ti}^{TiB_2} > \mu_{Ti}^{TiB_2 \rightleftharpoons \alpha-Ti}$ for x_1, which is also equivalent to the condition $G_2 < G_1$ (formation of α-Ti).

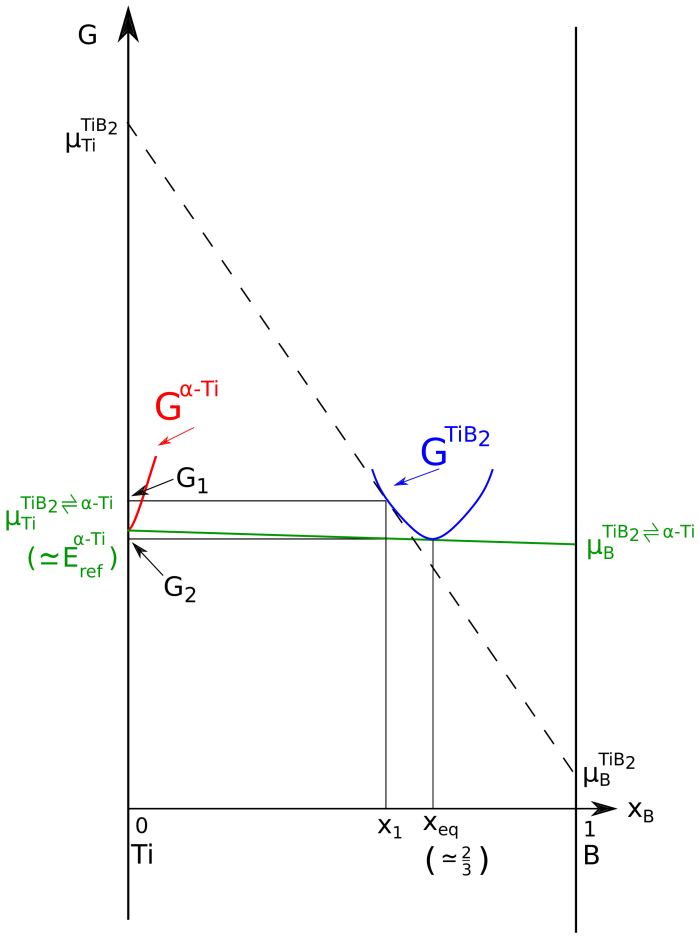

Figure B.2. Gibbs free energies G (in eV/atom) of α-B12 and TiB_2 phases as a function of the boron composition in the Ti-B system. The equilibrium chemical potentials of Ti and B noted $\mu_{Ti}^{TiB_2 \rightleftharpoons \alpha-B12}$ and $\mu_B^{TiB_2 \rightleftharpoons \alpha-B12}$ are given by the common tangent (green line). The Gibbs free energy of TiB_2 at composition x_2 is noted G_3. For the same composition, the common tangent gives the Gibbs free energy G_4 of the mixture of α-B12 and TiB_2 at equilibrium. $G_4 < G_3$ implies the formation of α-B12 from TiB_2. The tangent to G_{TiB_2} at composition x_2 (dotted line) gives the chemical potentials $\mu_{Ti}^{TiB_2}$ and $\mu_B^{TiB_2}$ in TiB_2 at this composition. It can be seen that $\mu_{Ti}^{TiB_2} < \mu_{Ti}^{TiB_2 \rightleftharpoons \alpha-B12}$ for x_2, which is also equivalent to the condition $G_4 < G_3$ (formation of α-B12).

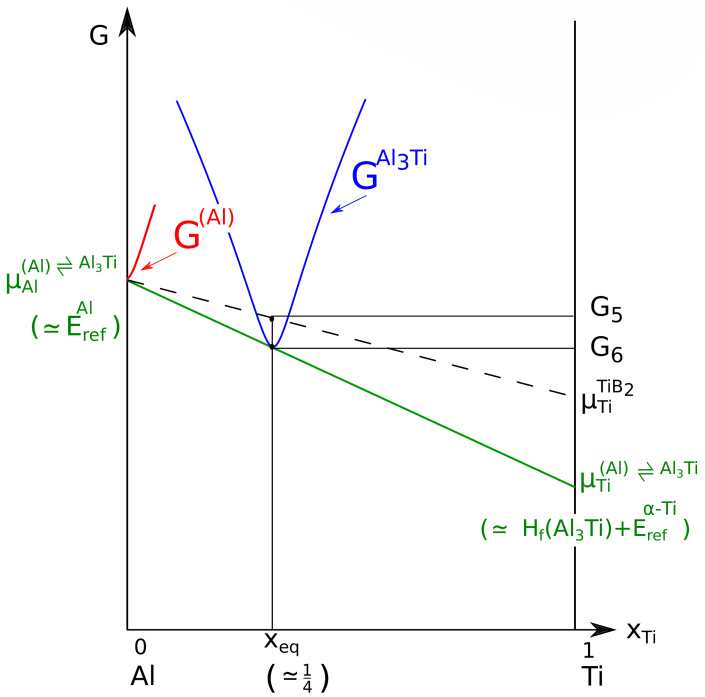

Figure B.3. Gibbs free energies G (in eV/atom) of the solid solution (Al) and Al_3Ti as a function of the Ti composition in the Al-Ti system. The green line stands for the common tangent. Its intersections with the axes $x_{Ti} = 0$ and $x_{Ti} = 1$ give respectively the equilibrium chemical potentials of Al and Ti noted $\mu_{Al}^{(Al) \rightleftharpoons Al_3Ti}$ and $\mu_{Ti}^{(Al) \rightleftharpoons Al_3Ti}$. The Gibbs free energy of Al_3Ti at its equilibrium composition x_{eq} with (Al) is noted G_6. For the same composition, the dotted line gives the energy G_5 of a mixture of Al and Ti atoms present respectively in the (Al) and TiB_2 phases at the chemical potentials $\mu_{Al}^{(Al) \rightleftharpoons Al_3Ti}$ and $\mu_{Ti}^{TiB_2}$. Since $G_6 < G_5$, the formation of Al_3Ti from (Al) and TiB_2 is promoted. It is equivalent to the condition $\mu_{Ti}^{(Al) \rightleftharpoons Al_3Ti} < \mu_{Ti}^{TiB_2}$.

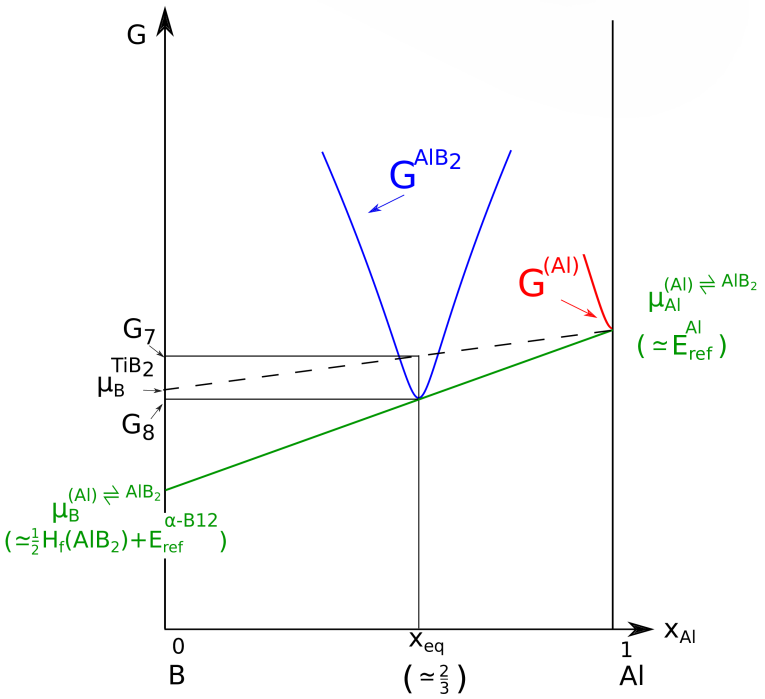

Figure B.4. Gibbs free energies G (in eV/atom) of the solid solution (Al) and AlB_2 as a function of the Al composition in the B-Al system. The green line stands for the common tangent. Its intersections with the axes $x_{Al} = 0$ and $x_{Al} = 1$ give respectively the equilibrium chemical potentials of B and Al noted $\mu_B^{(Al)\rightleftharpoons AlB_2}$ and $\mu_{Al}^{(Al)\rightleftharpoons AlB_2}$. The Gibbs free energy of AlB_2 at its equilibrium composition x_{eq} with (Al) is noted G_8. For the same composition, the dotted line gives the energy G_7 of a mixture of Al and B atoms present respectively in the (Al) and TiB_2 phases at the chemical potentials $\mu_{Al}^{(Al)\rightleftharpoons AlB_2}$ and $\mu_B^{TiB_2}$. Since $G_8 < G_7$, the formation of AlB_2 from (Al) and TiB_2 is promoted. It is equivalent to the condition $\mu_B^{(Al)\rightleftharpoons AlB_2} < \mu_B^{TiB_2}$.

C Effect of Al deformation on surface energies and interface energies

Table C.1. Interface energies σ (in mJ/m^2) in Ti-rich conditions ($\Delta\mu_{\mathrm{Ti}} = -1.594\ eV$) obtained for the different configurations by considering the surface energy of the deformed Al slab due to the coherent interface.

Configuration	PBC	FSC1	FSC2
I1	2374 ± 37[a]	2550 ± 30	2284
I2	785 ± 17	835 ± 44 (1450 [20])	739 ± 173 (1000 [21])
I3	794 ± 18	800 ± 70	774 ± 34
I4	1838 ± 23	1943 ± 50 (3000 [20])	1836 ± 41
I5	2028 ± 19	2081 ± 11	2050 ± 102 (2860 [21])
I6	2155 ± 14	2213 ± 41	2163 ± 52
MT Ti	793 ± 13	834 ±244	754 ± 8
MT B1	1845 ± 26	1899 ±16	1902 ± 7
MT B2	2151 ± 34	2281 ± 76	2023 ± 271

a. Uncertainty obtained from linear regression

Table C.2. Interface energies σ (in mJ/m^2) in B-rich conditions ($\Delta\mu_{\mathrm{Ti}} = -3.043\ eV$) obtained for the different configurations by considering the surface energy of the deformed Al slab due to the coherent interface.

Configuration	PBC	FSC1	FSC2
I1	3669 ± 40[a]	3920 ± 34	3572
I2	2065 ± 17	2165 ± 50 (3228 [20])	2049 ± 189 (2826 [21])
I3	2086 ± 20	2150 ± 76	2080 ± 37
I4	547 ± 21	598 ± 50 (1030 [20])	522 ± 44
I5	749 ± 17	765 ± 11	746 ± 87 (1780 [21])
I6	864 ± 14	881 ± 39	865 ± 50
MT Ti	2085 ± 15	2183 ±256	2044 ± 14
MT B1	555 ± 24	561 ±17	618 ± 2
MT B2	863 ± 34	946 ± 69	745 ± 271

a. Uncertainty obtained from linear regression

D Dispersion of χ values in the simulations

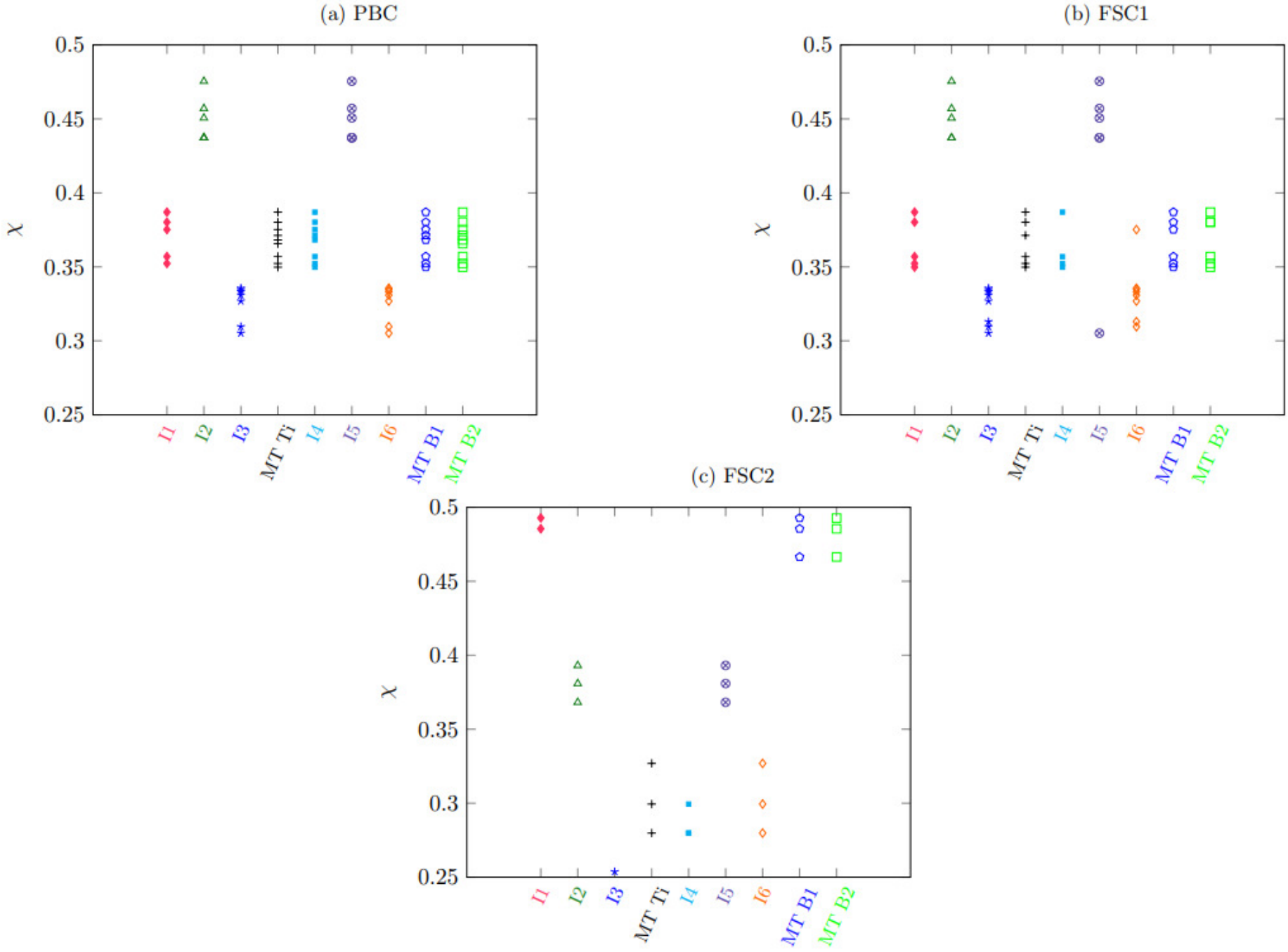

Figure D.1. Volume fraction χ dispersion of each configuration for PBC, FSC1 and FSC2 systems.

E Work of adhesion

According to [20, 21], the stability of the Al/TiB_2 interfaces can be deduced from the work of adhesion. In [20], it is defined as follows:

$$W_{ad}^{FSC1}(\chi, p) = \frac{1}{A}(E_{tot}^{Al} + E_{tot}^{TiB_2} - E_{tot}^{Al/TiB_2}) \tag{E.1}$$

whereas in [21]:

$$W_{ad}^{FSC2}(\chi, p) = \frac{1}{2A}(2E_{tot}^{Al} + E_{tot}^{TiB_2} - E_{tot}^{Al/TiB_2}) \tag{E.2}$$

Its definition then depends on the choice of the FSC1 or FSC2 systems used to calculate it. By injecting equations (6) and (11) in equation (E.1), W_{ad}^{FSC1} becomes:

$$AW_{ad}^{FSC1}(\chi, p) = (2A\gamma^{Al} + n_{Al}\mu_{Al}) + (2A\gamma^{TiB_2} + n_{Ti}\mu_{Ti}^{TiB_2} + n_B\mu_B^{TiB_2}) - (\Delta E_{multi}(p, \chi) + \sum_i n_i\mu_i) \tag{E.3}$$

By reporting equation (9) in equation (E.3) and after simplification of the chemical potential terms, the following relation between W_{ad}^{FSC1} and σ^{FSC1} is obtained:

$$W_{ad}^{FSC1}(\chi, p) = (\gamma^{Al} + \gamma^{TiB_2}) - \sigma^{FSC1} - \frac{1}{A}e_{el}(\chi)V_l p \tag{E.4}$$

Similar expression can be established for the work of adhesion in FSC2 systems:

$$W_{ad}^{FSC2}(\chi, p) = (\gamma^{Al} + \gamma^{TiB_2}) - \sigma^{FSC2} - \frac{1}{2A}e_{el}(\chi)V_l p \tag{E.5}$$

In principles equations (E.4) and (E.5) show that for the same values of p, χ, γ^{TiB_2} and γ^{Al}, it is equivalent to determine the most stable configuration by searching for the minimum of σ (interface energy criterion) or the maximum of W_{ad} (work of adhesion criterion). Namely between two configurations for a given Ti or B termination the following equality holds $\Delta W_{ad} = -\Delta\sigma$. The values of W_{ad}^{FSC1} and W_{ad}^{FSC2} are calculated in this work with the same number of Al and TiB_2 layers as in [20, 21] and reported in Tables E.1 and E.2 for all the configurations. Values of σ are recalled in these tables in order to compare the results given by the different criteria. Moreover, W_{ad}^{FSC1} and W_{ad}^{FSC2} obtained respectively in [20] and [21] are indicated for discussion.

Table E.1. Relative stabilities of Ti and B-terminated configurations for FSC1 systems predicted by the interface energy and work of adhesion criteria. Top (respectively down) configurations of the table correspond to the most (respectively least) stable ones. Interface energies σ are given for $\Delta\mu_{\mathrm{Ti}}$ =-1.594 eV. All values in brackets are in J/m^2.

	This work			Han et al. [20]
	σ^{FSC1}	$\mathrm{W}_{\mathrm{ad}}^{\mathrm{FSC1}}(\chi=0.52,p=12)$	$\mathrm{W}_{\mathrm{ad}}^{\mathrm{FSC1}}+\frac{1}{A}e_{\mathrm{el}}(\chi)V_l p$	$\mathrm{W}_{\mathrm{ad}}^{\mathrm{FSC1}}(\chi=0.52,p=12)$
Ti-terminated	MT Ti (0.83) I3 (0.85) I2 (0.90) I1 (2.58)	I3 (2.70) I2 (2.68) MT Ti (2.46) I1 (1.13)	MT Ti (3.20) I3 (3.18) I2 (3.13) I1 (1.44)	I2,I3,MT Ti (3.18) I1 (3.17)
B-terminated	MT B1 (1.96) I4 (1.99) I5 (2.16) I6 (2.28) MT B2 (2.34)	I4 (2.34) MT B1 (2.20) I5 (2.11) MT B2 (2.03) I6 (2.03)	MT B1 (2.74) I4 (2.71) I5 (2.54) I6 (2.42) MT B2 (2.36)	I4 (2.77) MT B1 (2.44) I5,I6 (2.43)

Table E.2. Relative stabilities of Ti-terminated configurations for FSC2 systems with the interface energy and work of adhesion criteria. Top (respectively down) configurations of the table correspond to the most (respectively least) stable ones. Interface energies σ are given for $\Delta\mu_{\mathrm{Ti}}$ =-1.594 eV. All values in brackets are in J/m^2.

	This work			Deng et al. [21]
	σ^{FSC2}	$\mathrm{W}_{\mathrm{ad}}^{\mathrm{FSC2}}(\chi=0.58,p=19)$	$\mathrm{W}_{\mathrm{ad}}^{\mathrm{FSC2}}+\frac{1}{2A}e_{\mathrm{el}}(\chi)V_l p$	$\mathrm{W}_{\mathrm{ad}}^{\mathrm{FSC2}}(\chi=0.58,p=19)$
Ti-terminated	I2 (0.78) I3 (0.82) MT Ti (0.83) I1 (2.36)	MT Ti (2.72) I3 (2.45) I2 (2.40) I1 (1.00)	I2 (3.22) MT Ti,I3 (3.18) I1 (1.64)	I2 (3.39) MT Ti (3.38) I1 (3.24) I3 (3.1)
B-terminated	I4 (1.88) MT B1 (1.99) I5 (2.10) MT B2 (2.12) I6 (2.23)	I4 (2.25) MT B1 (2.18) MT B2 (2.05) I6 (1.83) I5 (1.82)	I4 (2.79) MT B1 (2.66) I5 (2.55) MT B2 (2.53) I6 (2.43)	MT B2,I5 (2.24) I4 (2.11) I6 (1.87)

References

[1] A. Sreenivasan, S.P. Vizhian, N.D. Shivakumar, M. Muniraju, and M. Raguraman. A study of microstructure and wear behaviour of TiB_2/Al metal matrix composites. *Latin American Journal of Solids and Structures*, 8:1–8, 2011.

[2] Y. Ma, G. Ji, Z. Chen, A. Addad, and V. Ji. On the study of a TiB_2 nanoparticle reinforced 7075al composite with high tensile strength and unprecedented ductility. In *THERMEC 2018*, volume 941 of *Materials Science Forum*, pages 1933–1938. Trans Tech Publications Ltd, 2019.

[3] M. Yu, A. Addad, J. Gang, M.X. Zhang, W. Lefebvre, Z. Chen, and V. Ji. Atomic-scale investigation of the interface precipitation in a TiB_2 nanoparticles reinforced Al–Zn–Mg–Cu matrix composite. *Acta Materialia*, 185:287–299, 2020.

[4] Y. Zhao, X. Liao, S. Cheng, E. Ma, and Y. Zhu. Simultaneously increasing the ductility and strength of nanostructured alloys. *Advanced Materials*, 18:2280–2283, 2006.

[5] X.P. Li, G. Ji, Z. Chen, A. Addad, Y. Wu, H.W. Wang, J. Vleugels, J. Van Humbeeck, and J.P. Kruth. Selective laser melting of nano-TiB_2 decorated AlSi10Mg alloy with high fracture strength and ductility. *Acta Materialia*, 129:183–193, 2017.

[6] P. V. Liddicoat, X.Z. Liao, Y. Zhao, Y. Zhu, M. Y. Murashkin, E. J. Lavernia, R. Z. Valiev, and S. P. Ringer. Nanostructural hierarchy increases the strength of aluminium alloys. *Nature Communications*, 1:1–7, 2010.

[7] J. H. Martin, B. D. Yahata, J. M. Hundley, J. A. Mayer, T. A. Schaedler, and T. M. Pollock. 3D printing of high-strength aluminium alloys. *Nature*, 549:365–369, 2017.

[8] Z. Li, Q. Guo, Z. Li, G. Fan, D.B. Xiong, Y. Su, J. Zhang, and D. Zhang. Enhanced mechanical properties of graphene (reduced graphene oxide)/aluminum composites with a bioinspired nanolaminated structure. *Nano Letters*, 15:8077–8083, 2015.

[9] X. Kai, Z. Li, G. Fan, Q. Guo, Z. Tan, W. Zhang, Y. Su, W. Lu, W.J. Moon, and D. Zhang. Strong and ductile particulate reinforced ultrafine-grained metallic composites fabricated by flake powder metallurgy. *Scripta Materialia*, 68:555–558, 2013.

[10] Y. Mishin, M. Asta, and Ju Li. Atomistic modeling of interfaces and their impact on microstructure and properties. *Acta Materialia*, 58(4):1117–1151, 2010.

[11] S.Y. Hu, M.I. Baskes, M. Stan, and L.Q. Chen. Atomistic calculations of interfacial energies, nucleus shape and size of precipitates in Al-Cu alloys. *Acta Materialia*, 54:4699–4707, 2006.

[12] X.J. Ye, C.S. Liu, W. Zhong, and Y.W. Du. Precipitate size dependence of Ni/Ni_3Al interface energy. *Physics Letters A*, 379:37–40, 2015.

[13] V. Vaithyanathan, C. Wolverton, and L.Q. Chen. Multiscale modeling of precipitate microstructure evolution. *Physical Review Letters*, 88:125503–125503, 2002.

[14] V. Vaithyanathan, C. Wolverton, and L.Q. Chen. Multiscale modeling of precipitation θ' in Al-Cu binary alloys. *Acta Materialia*, 52:2973–2987, 2004.

[15] L. Thuinet and R. Besson. Ab initio study of competitive hydride formation in zirconium alloys. *Intermetallics*, 20:24–32, 2012.

[16] M.A. Louchez, R. Besson, L. Thuinet, and A. Legris. Interfacial properties of hydrides in alpha-Zr: a theoretical study. *Journal of Physics: Condensed Matter*, 29:415001–415001, 2017.

[17] Y. Wang, Z.-K. Liu, L.Q. Chen, and C. Wolverton. First-principles calculations of Mg_5Si_6/Al interfaces. *Acta Materialia*, 55(17):5934–5947, 2007.

[18] W. Zhang, D. Xiao, and D. Ding. A first-principles investigation of interfacial properties and electronic structure of SiO_2/Al interface. *Computational Materials Science*, 188:110228, 2021.

[19] L. Rui, Y. Xiaoming, F. Kaixuan, and X. Ru. First-principles calculations on Mg/TiB_2 interfaces. *Computational Materials Science*, 149:373–378, 2018.

[20] Y. Han, Y. Dai, D. Shu, J. Wang, and B. Sun. First-principles calculations on the stability of Al/TiB_2 interface. *Applied Physics Letters*, 89:144107–144107, 2006.

[21] C. Deng, B. Xu, P. Wu, and Q. Li. Stability of the Al/TiB_2 interface and doping effects of Mg/Si. *Applied Surface Science*, 425:639–645, 2017.

[22] H.L. Zhang, Y.F. Han, Y.B. Dai, J. Wang, and B.D. Sun. An ab initio molecular dynamics study: liquid-Al/solid-TiB_2 interfacial structure during heterogeneous nucleation. *Journal of Physics D: Applied Physics*, 45:455307, 2012.

[23] H.L. Zhang, Y.F. Han, Y.B. Dai, S.S. Lu, J. Wang, J. Zhang, D. Shu, and B.D. Sun. An ab initio study on the electronic structures of the solid/liquid interface between TiB_2 (0001) surface and Al melts. *Journal of Alloys and Compounds*, 615:863–867, 2014.

[24] Y. Han, Y. Dai, D. Shu, J. Wang, and B. Sun. First-principles study of TiB_2 (0001) surfaces. *Journal of Physics: Condensed Matter*, 18:4197–4205, 2006.

[25] G. Kresse and J. Furthmüller. Efficient iterative schemes for ab initio total-energy calculations using a plane-wave basis set. *Physical Review B*, 54:11169–11186, 1996.

[26] J.P. Perdew, K. Burke, and M. Ernzerhof. Generalized gradient approximation made simple. *Physical Review Letters*, 77:3865–3868, 1996.

[27] H.J. Monkhorst and J.D. Pack. Special points for brillouin-zone integrations. *Physical Review B*, 13:5188–5192, 1976.

[28] P. E. Blöchl. Projector augmented-wave method. *Physical Review B*, 50:17953–17979, 1994.

[29] K. Momma and F. Izumi. *VESTA3* for three-dimensional visualization of crystal, volumetric and morphology data. *Journal of Applied Crystallography*, 44:1272–1276, 2011.

[30] A.A. Abdel-Hamid, S. Hamar-Thibault, and R. Hamar. Crystal morphology of the compound TiB_2. *Journal of Crystal Growth*, 71:744–750, 1985.

[31] M.E Straumanis. The precision determination of lattice constants by the powder and rotating crystal methods and applications. *Journal of Applied physics*, 20:726–734, 1949.

[32] H.H. Xiong, H.N. Zhang, and J.H Dong. Adhesion strength and stability of TiB_2/TiC interface in composite coatings by first principles calculation. *Computational Materials Science*, 127:244–250, 2017.

[33] Y. Zhou, H. Xiong, Y. Yin, and S. Zhong. First principles study of surface properties and oxygen adsorption on the surface of Al_3Ti intermetallic alloys. *RSC Advances*, 9:1752–1758, 2019.

[34] K.S. Kumar. X-ray peak intensities for the binary compound Al_3Ti. *Powder Diffraction*, 5:165–166, 1990.

[35] F.S. Meng, Z. Yao, M. Všianská, M. Friák, and M. Šob. Theoretical investigations on structural, elastic, thermodynamic and electronic properties of Al_3Ti and Al_3V compounds in $L1_2$ structure under high pressure. *Materials Research Express*, 6:56536–56555, 2019.

[36] T.E. Quested. Understanding mechanisms of grain refinement of aluminium alloys by inoculation. *Materials Science and Technology*, 20:1357–1369, 2004.

[37] M.X. Zhang, P.M. Kelly, M.A. Easton, and J.A. Taylor. Crystallographic study of grain refinement in aluminum alloys using the edge-to-edge matching model. *Acta Materialia*, 53:1427–1438, 2005.

[38] M. Easton and D. StJohn. Grain refinement of aluminum alloys: Part I. the nucleant and solute paradigms—a review of the literature. *Metallurgical and Materials Transactions A*, 30:1613–1623, 1999.

[39] C. Wolverton and V. Ozoliņš. Entropically favored ordering: The metallurgy of Al_2Cu revisited. *Physical Review Letters*, 86:5518–5521, 2001.

[40] J.C. Boettger. Nonconvergence of surface energies obtained from thin-film calculations. *Physical Review B*, 49:16798–16800, 1994.

[41] V. Fiorentini and M. Methfessel. Extracting convergent surface energies from slab calculations. *Journal of Physics: Condensed Matter*, 8:16525–6529, 1996.

[42] L. Zhang, Q. Zheng, H. Jiang, and J. Zhao. Interfacial energy between Al melt and TiB_2 particles and efficiency of TiB_2 particles to nucleate α-Al. *Scripta Materialia*, 160:25–28, 2019.

[43] R. Besson. Point defects in multicomponent ordered alloys: Methodological issues and working equations. *Acta Materialia*, 58:379–385, 2010.

[44] R. Besson and L. Favergeon. Understanding the Mechanisms of CaO Carbonation: Role of Point Defects in $CaCO_3$ by Atomic-Scale Simulations. *The Journal of Physical Chemistry C*, 118(39):22583–22591, 2014.

[45] J. Kwon, L. Thuinet, M. N. Avettand-Fenoèl, A. Legris, and R. Besson. Point defects and formation driving forces of complex metallic alloys: Atomic-scale study of Al_4Cu_9. *Intermetallics*, 46:250, 2014.

[46] R. Besson. Understanding phase equilibria in high-entropy alloys: II. Atomic-scale study of incorporation of metallic elements in Cr carbides - Application to equilibrium with AlCrFeMnMo. *Journal of Alloys and Compounds*, 874:159959, 04 2021.

[47] C. Thenot, R. Besson, P. Sallot, J.-P. Monchoux, and D. Connétable. Interactions of oxygen with intrinsic defects in L10 -TiAl in presence of substitutional solutes: Influence on diffusion kinetics. *Computational Materials Science*, 201:110933, 2022.

[48] L. Shao, T.T. Shi, J. Zheng, H.C. Wang, X.Z. Pan, and B.Y. Tang. First-principles study of point defects in C14 $MgZn_2$ laves phase. *Journal of Alloys and Compounds*, 654:475–481, 2016.

[49] Y.H. Duan, Y. Sun, Z.Z. Guo, M.J. Peng, P.X. Zhu, and J.H. He. Elastic constants of AlB_2-type compounds from first-principles calculations,. *Computational Materials Science*, 51:112–116, 2019.

[50] P. Vallars. *Pearson's Handbook Crystallographic Data for Intermetallic Phases*. ASM, International, Materials Park, OH, 1997.

[51] Y.S. Touloukian, R.K. Kirby, R.E. Taylor, and T.Y.R. Lee. *Thermophysical Properties of Matter v.12 : Thermal Expansion; Metallic Elements and Alloys*, volume 12. Plenum, New york, 1975.

[52] W. Li and T. Wang. Ab initio investigation of the elasticity and stability of aluminium. *Journal of Physics: Condensed Matter*, 10:9889–9904, 1998.

[53] J. Vallin, M. Mongy, K. Salama, and O. Beckman. Elastic constants of aluminum. *Journal of Applied Physics*, 35:1825–1826, 1964.

[54] K.B. Panda and K.S. Ravi Chandran. Determination of elastic constants of titanium diboride (TiB_2) from first principles using FLAPW implementation of the density functional theory. *Computational Materials Science*, 35:134–150, 2006.

[55] P.S. Spoor and J.D. Maynard. Elastic constants and crystal anisotropy of titanium diboride. *Applied Physics Letters*, 70:1959–1961, 1997.

[56] H. Ledbetter and T. Takaho. Elastic-stiffness coefficients of titanium diboride. *Journal of research of the National Institute of Standards and Technology*, 114:333–339, 2009.

[57] R. Liu, X. Yin, K. Feng, and R. Xu. First-principles calculations on Mg/TiB_2 interfaces. *Computational Materials Science*, 149:373–378, 2018.